Chair of Material Physics

Master's Thesis

Influence of Cold Rolling on the Fatigue Crack Growth Behavior of Tungsten

Simon Pillmeier, BSc

March 2020

EIDESSTATTLICHE ERKLÄRUNG

Ich erkläre an Eides statt, dass ich diese Arbeit selbständig verfasst, andere als die angegebenen Quellen und Hilfsmittel nicht benutzt, und mich auch sonst keiner unerlaubten Hilfsmittel bedient habe.

Ich erkläre, dass ich die Richtlinien des Senats der Montanuniversität Leoben zu "Gute wissenschaftliche Praxis" gelesen, verstanden und befolgt habe.

Weiters erkläre ich, dass die elektronische und gedruckte Version der eingereichten wissenschaftlichen Abschlussarbeit formal und inhaltlich identisch sind.

Datum 09.03.2020

Unterschrift Verfasser
Simon, Pillmeier

Abstract

Tungsten possesses the highest melting point of all metals and has excellent high temperature tensile and creep strength, chemical resistance against molten metals, molten salts and most acids. Therefore, the use as a structural material in high temperature applications (e.g. for cooling pipes in fusion reactors) is desirable. So far the limiting factor was its high ductile to brittle transition temperature paired with poor fracture toughness at ambient temperatures. It was shown that severe plastic deformation such as severe cold rolling could not only increase strength, but also improve ductility and toughness of tungsten. In this work, the influence of cold rolling on the fatigue crack growth (FCG) behavior was investigated. Therefore, tungsten sheets with three different thicknesses (2 mm, 1mm and 100 μm) corresponding to different degrees of deformation were selected to prepare compact-tension (CT) and single edge notched tension (SENT) specimens. To account for orientation influences the crack propagation direction parallel, perpendicular and under 45° to the rolling direction was selected. It could be shown that a pronounced cyclic R-curve behavior evolves, leading to high threshold stress intensity factor ranges ΔK_{th}, even at high load ratios. Furthermore, a pronounced anisotropy of the FCG behavior was observed where the crack growth direction perpendicular to the rolling direction exhibits the highest ΔK_{th} and the lowest crack growth-rates. Especially the tungsten foils with 100 μm thickness showed remarkable FCG behavior with a pronounced Paris-regime. As a consequence, tungsten qualifies as a good candidate for the utilization as a laminate material applicable for structural applications.

Zusammenfassung

Wolfram besitzt den höchsten Schmelzpunkt aller Metalle und verfügt über eine ausgezeichnete Hochtemperaturfestigkeit und Kriechfestigkeit, chemische Beständigkeit gegen geschmolzene Metalle, geschmolzene Salze und die meisten Säuren. Daher ist die Verwendung als Konstruktionswerkstoff in Hochtemperaturanwendungen (z.B. für Kühlrohre in Fusionsreaktoren) wünschenswert. Bisher war der begrenzende Faktor seine hohe Spröd-duktil-Übergangstemperatur gepaart mit einer schlechten Bruchzähigkeit bei Umgebungstemperaturen. Es konnte gezeigt werden, dass eine plastische Hochverformung wie z.B. starkes Kaltwalzen nicht nur die Festigkeit, sondern auch die Duktilität und Zähigkeit von Wolfram verbessern kann. In dieser Arbeit wurde der Einfluss des Kaltwalzens auf das Verhalten des Ermüdungsrisswachstums (FCG) untersucht. Daher wurden Wolframbleche mit drei verschiedenen Dicken (2 mm, 1 mm und 100 µm), die unterschiedlichen Verformungsgraden entsprechen, ausgewählt, um Compact-Tension (CT)- und Single-Edge-Notched Tension (SENT)-Proben herzustellen. Zur Berücksichtigung von Orientierungseinflüssen wurde die Rissausbreitungsrichtung parallel, senkrecht und unter 45° zur Walzrichtung gewählt. Es konnte gezeigt werden, dass sich ein ausgeprägtes zyklisches R-Kurven-Verhalten entwickelt, das selbst bei hohen Lastverhältnissen zu hohen Schwellenspannungsintensitätsfaktorbereichen ΔKth führt. Darüber hinaus wurde eine ausgeprägte Anisotropie des FCG-Verhaltens beobachtet, wobei die Risswachstumsrichtung senkrecht zur Walzrichtung die höchsten ΔKth und die niedrigsten Risswachstumsraten aufweist. Insbesondere die Wolframfolien mit 100 µm Dicke zeigten ein bemerkenswertes FCG-Verhalten mit einem ausgeprägten Paris-Bereich. Folglich ist Wolfram ein guter Kandidat für den Einsatz als Laminatmaterial für strukturelle Anwendungen.

Table of Contents

1. Introduction

1.1 Properties and Applications of Tungsten [1,2]

Tungsten has the highest melting point of all metals of about 3695 K and is therefore regarded as a refractory metal. Correlated to that is also its exceptionally high Young´s Modulus of 405 GPa at room temperature. The high melting point makes it possible to operate tungsten at relatively low homologous temperatures and thus exhibits high strength and high creep resistance at elevated temperatures. Other superior properties are low vapor pressure, high thermal shock resistance, high thermal conductivity and high erosion resistance. It also shows good corrosion performance against most acids, leaches, molten metals, oxides and gases even and high temperatures. One major drawback is its high affinity to oxygen at temperatures above 500°C making it necessary to provide inert atmospheres at these temperatures. Another downside for many applications is its high density of 19.25 g/cm^3. Exceptions are uses as ballistic material for military purposes or due to the similar density as gold (19.3 g/cm^3) and much lower price as substitute for gold.

Because of its superior properties tungsten is mostly used when extreme temperatures prevail. Typical applications are: rotating anode in x-ray tubes, light bulb filaments, electrode in gas tungsten arc welding and as vessel in sapphire single-crystal growth [1,2]. These application make use of tungsten more as a functional material rather than as structural material. Or in other words: the mechanical loads are not demanding and the tungsten parts only need to stay in their shape. However, because of its excellent high temperature properties and chemical resistance it is very desirable to use tungsten also as a structural material. Potential application would be as cooling pipes for innovative high temperature power conversion systems [3]. One example is the use in concentrated solar power. Here large mirrors are used to concentrate the light from the sun to a receiver, which is mostly realized as a tower where the heat is transferred by cooling pipes to an engine. The medium for the heat flux can be water/steam, molten salts, pressurized air or helium with fluid temperatures ranging from 300 °C for water and up to 900 °C for pressurized air [3]. The idea behind the realization of these pipes is to roll up a tungsten laminate material that consist of thin tungsten foils filled with an interlayer material. More details on these laminates will be given in a later section, as well as the problems that arise for the use of tungsten as structural material. Tungsten is also a very promising candidate for use in fusion power plants. The basic theory of fusion and the implementation of tungsten together with the challenges will be given in the next section.

1.2 Nuclear Fusion and Tungsten

In the early 20th century it was discovered that nuclear fusion was the energy source that powers stellar objects such as our sun. In the sun´s core light elements like hydrogen combine to create helium at temperatures of about 15,000,000°C and estimated pressures of 26 10^{15} Pa [4]. Since then scientists and engineers try to harvest this form of energy by recreating a fusion reaction here on earth. Sadly, the most successful application so far was the atomic bomb. But extensive work is put into the development of a fusion power plant to generate electric power for civil use.

The basic principle of fusion is that energy is released when two light elements merge to form a heavier element. The mass of this resulting element is slightly lower than the sum of the two light elements. This holds to be true up to iron (Fe). The difference in mass is converted into energy by Einstein´s formula $\Delta E = \Delta m * c^2$. The most efficient reaction in laboratory settings is found to be between the two isotopes of hydrogen deuterium (D) and tritium (T) to form helium where the highest amount of energy is gained at the lowest temperature. As seen in Figure 1 not only helium is formed but also a high energy neutron. The big challenge lies in the high temperature and pressure required to overcome the repellent forces of the atomic nuclei to start the fusion reaction. Many different strategies have been proposed to reach these conditions. One way is to heat the fusion fuel (D and T) to sufficient temperatures so it becomes a plasma inside a toroidal vacuum chamber and is then further heated and confined using magnetic fields. Depending on the shape of the magnetic field there are two main designs: the Tokamak and the Stellarator. In the past experimental fusion reactors employing a Tokamak concept have shown to have a higher fusion triple point (also known as Lawson criterion) that has risen steadily over the last decades. The Lawson criterion is a combination of plasma temperature, density and confinement time. Above a certain limit the fusion reaction yields more energy than it consumes and becomes self-sustaining - the fusion reaction is ignited. Currently a new Tokamak reactor is build called ITER (International thermonuclear experimental
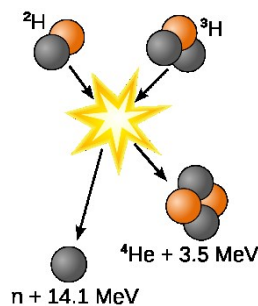

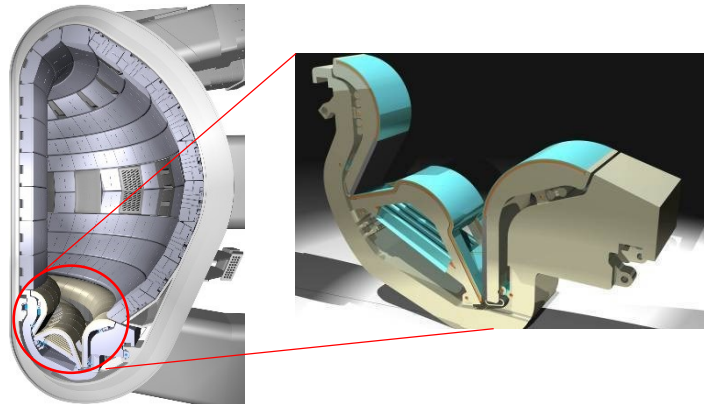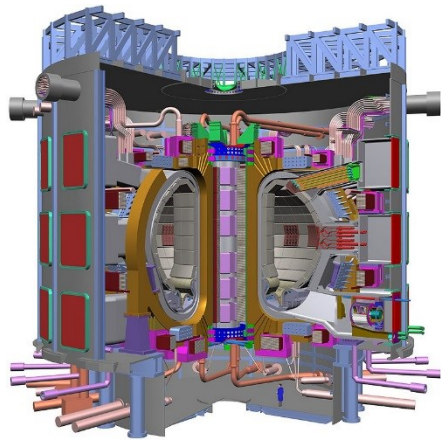*Figure 1: The D-T fusion reaction, it yields the highest energy* [4]

Figure 3: Cross section of an ITER model, it will be the biggest experimental fusion reactor [4]   *Figure 2: Detailed view of the vacuum chamber of ITER and a divertor cassette* [4]

reactor). It will be the biggest fusion reactor ever realized and is projected to fulfill the Lawson criterion and produce more power than it is used to heat the plasma. A cross section of a model of ITER can be seen in Figure 3. In both designs (Tokamak and Stellarator) sufficient shielding of the vacuum chamber (seen in Figure 2) from the plasma is needed. The inner wall is often called "first wall" and is required to shield the structure behind it from the intense neutron radiation and thereby transfering the energy of the neutron into heat. Cooling pipes behind the walls carry the heat away and is converted into electricity using a steam turbine and a generator. In the future the first wall will also be used to breed the tritium that is needed as fusion fuel [4]. Because tungsten has a low sputter yield, high heat conductivity and high temperature strength, it is an optimal candidate to be used as first wall material in these harsh conditions. Another essential part of the tokamak is the "divertor" at the bottom of the vacuum chamber, Figure 3. The main purpose of it is to extract the so called fusion ash and other contaminations in the plasma. At steady state it is subjected to a heat flux of 10 MW/m^2 and can rise to 20 MW/m^2. Here tungsten is also used as an armor material. In addition tungsten is also considered as structural material for the cooling pipes of the divertor that would be operated with helium at 600 °C and 100 bar [3].

The use of tungsten as a structural material is limited by its brittleness, however, under certain conditions it can be overcome, which will be described in the next section.

1.3 Ductilization Strategies for Tungsten

Since tungsten has a high affinity to oxygen at elevated temperatures (e.g. above 770K [2]) inert atmospheres are needed during processing and manufacturing of tungsten parts. This requirement is often complicated to be implemented and therefore costly most of the times. Hence, processing temperature at ambient temperatures would be beneficial. However, typical of most body centered cubic (bcc) metals, tungsten experiences a transition from brittle behavior at low temperatures to ductile behavior at high temperatures. The main problem for the use of tungsten in fusion applications or in general as structural material is its high brittle to ductile transition temperature (DBTT) which is dependent on the strain-rate [5], the material condition (microstructure and alloying) and testing direction [6]. Values of the DBTT typically range between 400K and 950K, and thus this metal exhibits low toughness and plasticity values at room temperature (RT). Therefore, the main goal of the research efforts is to shift the DBTT below RT to simplify the processing of tungsten and thereby reduce the costs. Researchers have come up with different approaches to increase the ductility of tungsten which will be described below.

1.3.1 Alloying

The most important alloying element for the ductilization of tungsten is rhenium (Re) which was shown in the mid of the last century [7]. Re reaches its maximum solubility in W of 37 at% at 3000°C and decreases with temperature [8]. Commercially available alloys of this type are WRe5 and WRe26 with 5 wt% and 26 wt% rhenium respectively [2]. Raffo [9] showed that the BDTT could be lowered from around 550K for unalloyed tungsten to about 350K for tungsten with 25% rhenium. At first sight, one would expect that the W-Re alloys exhibit a solid solution strengthening effect, where the strength increases with increasing rhenium content. However, at temperatures below 280K this effect reverses and a softening effect is noticeable where the strength decreases with increasing rhenium content. This effect is not unique to the W-Re system and is also existent in other alloys (e.g. W-Ir [10]). Raffo also noticed a pronounced twin formation at lower temperatures in higher concentrated alloys. But it is unclear if this yields a positive effect on the ductility of the material. It was concluded that an increased dislocation mobility and thus an increased plasticity at the crack tip resulted in the lowered BDTT. More recent investigation used density function theory (DFT) calculations and revealed that alloying tungsten with rhenium leads to the transition of the non-planar ½ <111> screw dislocation from a symmetric core to an asymmetric core [11]. This causes a change in the preferred slip plane from {110} in pure tungsten to {112} in W-Re and also lowers the Peierls stress. The positive effect of Re arises from the excess electrons which fill the d-band and change the interatomic bonding. Similar simulations performed with tantalum and vanadium showed no

6

change in the screw dislocation core and therefore no significant change of ductility, which is in good agreement to experimental data. This also fits well with expectations since tantalum and vanadium are to the left of tungsten in the periodic table and therefore have no excess electrons. Fracture experiments performed by Gludovatz et al. confirm these findings [12]. Among others they tested WRe26 which exhibits fracture toughness values of about 54 MPam$^{1/2}$ at RT and increases with increasing temperature. Electron back scattered diffraction (EBSD) scans revealed pronounced plastic deformation along the crack path even at RT [12,13].

The main disadvantage that hinders the use of rhenium as a feasible ductilization strategy in the future is its rare abundance and therefore its high price.

1.3.2 Composite Materials: Fibre Reinforcement

The concept of fibre-reinforcement of brittle materials like ceramics is an adequate method to significantly enhance their toughness. One good example is silicon carbide reinforced with silicon carbide fibres (SiC$_f$/SiC), where the fracture toughness could be raised from about 2-4 MPam$^{1/2}$ [14] for pure SiC to about 25 MPam$^{1/2}$ [15] for the reinforced SiC. This concept was successfully transferred to tungsten, where drawn tungsten fibres coated with an engineered interface are embedded into a tungsten matrix. The interface is needed to provide a physical barrier between fibre and matrix and helps to maintain the composite structure during production and operation. Additionally, the interface must provide a load transfer and therefore should be as strong as possible. However, it is necessary that this bond breaks during the crack propagation so that toughening mechanisms can become active. Usually oxide coatings, i.e. ZrO_2, Er_2O_3 or WO_x are used as interface materials and are deposited using magnetron sputter deposition [16,17]. Tungsten composites are typically synthesized using a powder metallurgical route as this is the most advanced and most used technique. But the high pressures and temperatures used during the process can lead to a change of microstructure of the tungsten wires and therefore to a loss of the beneficial mechanical properties. An alternative production route uses a chemical vapor deposition (CVD) technique. Here tungsten is dissolved as tungsten hexafluoride (WF_6) and is reduced by hydrogen (H_2) in a heterogeneous surface reaction to produce a solid tungsten matrix. The main advantage of this technique is the considerably lowered process temperature. [18]

The idea behind this toughening strategy is not to improve the intrinsic crack growth resistance of the material itself but to introduce mechanisms of energy dissipation which act behind the crack tip and are therefore called extrinsic toughening effects [18]. As long as the tungsten fibres exhibit a ductile behavior, which is a result of the drawing process, their plastification acts as the main toughening mechanism. If the fibres recrystallize due to exposure to high temperatures, mechanisms as elastic bridging and fibre pull-

out become the domination toughening effects. As these later mechanisms are purely mechanical effects they would also be active if the material embrittles during operation in a fusion reactor due to neutron radiation and high heat flux. [16]

1.3.3 Grain Refinement by Cold Working

Grain refinement by cold working, e.g. cold rolling, is a common strategy to enhance the strength of metals. This is often accompanied by a significant loss of ductility and toughness. A few years ago it was recognized that some metals, when subjected to severe plastic deformation (SPD), for example, high pressure torsion (HPT) or equal channel angular pressing (ECAP), exhibit both, high strength and high ductility [19]. The grain size of the resulting microstructure is often below 100 nm, which is referred to as nano-crystalline. When metals are processed by means of SPD they also experience a loss of ductility at lower strains while the strength increased. Only when the degrees of strain get very high (e.g. multiple turns in the HPT process or several passes in the ECAP process) the ductility rises again while the strength increases or remains at a high level. Valiev et al. also noted a rise in strain-rate sensitivity [19].

The concept of SPD was then also introduced to tungsten by means of cold rolling by Wei et al. [20]. Cold-rolling is commonly referred to as rolling below the recrystallization temperature. It was found that by decreasing the rolling temperature, strength and ductility of tungsten can be increased significantly [20]. In this work a significantly reduced strain-rate sensitivity was noticed which is in agreement with other works, where no or only a slight strain-rate dependence of the DBTT was discovered [5]. A detailed study [21] on the microstructural evolution during the rolling process revealed that the grain size continuously decreases with increasing degree of deformation well down into the ultrafine grain (UFG) regime to about 240 nm in thickness direction for tungsten foils with 100 µm thickness. It is important to mention that the grains are not equiaxed. Due to the nature of the rolling process pancake-like grains are formed with the long axis parallel to the rolling direction. This grain refinement comes along with an increasing amount of high angle grain boundaries (HAGB) as the strain increases while the amount of low angle grain boundaries show no clear correlation with the degree of strain [21]. The cold rolling process also introduces a strong {100}<011> rotated cube texture, which seems to be an equilibrium condition as it does not change with further rolling below 100 µm thickness [21,22]. This microstructural anisotropy has consequences for the mechanical properties and the resulting effects will be discussed below.

As the rolled sheets become thinner and the degree of deformation rises the strength of tungsten increases continuously as the grains get smaller following a Hall-Petch relationship [23]. The foil with 100

µm thickness possesses an almost elastic-perfectly plastic tensile behavior. The ultimate tensile strength (UTS) was measured to be at 2300 MPa with an uniform elongation of around 1% and an elongation at fracture of about 2.5% at RT [23]. As there is almost no hardening the flow stress is just slightly below the UTS at about 2250 MPa. These values were all gained by tensile test were the tensile direction was parallel to the rolling direction (0° direction). When the tensile direction is rotated by 90° the strength at RT is similar but the ductility decreases dramatically and the specimen shows almost brittle fracture [24]. It was concluded that the anisotropic grain shape was the main reason for that behavior because the rotated cube texture is symmetrical in the plane and thus the crystals are orientated in the same way in both testing directions. This becomes more evident when testing at 600°C where the tensile curves for these two direction are nearly congruent [24]. A third testing direction between these two at an angle of 45° shows the most ductile behavior with an elongation at fracture of 4%. This is to be expected since the preferred slip direction of bcc metals is the <111> direction and in the 45° system due to the texture the highest shear stress lies parallel to the <111> crystallographic direction. Fracture mechanical investigations by Nikolic et al [25] on thin tungsten foils with 100 µm thickness revealed superior fracture behavior: a DBT at RT and fracture toughness values at RT of 94.8 MPam$^{1/2}$ for the T-L specimens, 105.9 MPam$^{1/2}$ for the L-T specimens and 64.3 MPam$^{1/2}$ for the 45° specimens were measured. The two letter code for the specimen orientation will be explained later. Even at -196 °C a fracture toughness of about 10-15 MPam$^{1/2}$ depending on the sample orientation was measured. At high temperatures the values seem to drop but this is due to the limitations of linear elastic fracture mechanics (LEFM). More advanced evaluation using the crack tip opening displacement (CTOD) [25] indicate a fracture toughness of about 115-120 MPam$^{1/2}$ at 800 °C for 45° specimens. These excellent values are the result of the prevailing microstructure with elongated grains that promotes toughening mechanisms related to delamination in the through-thickness of the foil.

It was also long believed that the positive effect of cold-working on the mechanical properties come from diluting impurities at the grain boundaries (GB). Like many bcc refractory metals tungsten is very sensitive to small interstitial atoms like oxygen, nitrogen or carbon that typically segregate to the grain boundaries due to a lack of solubility in the crystal. These elements usually weaken the GBs which will lead to intergranular failure during loading. When the grain size decreases the amount of GB-area naturally increases which in turn dilutes potentially present impurities. More recent studies suggest that grain size, grain shape and degree of deformation and therefore the dislocation density have a greater impact on the fracture resistance [26]. It was shown that deformation can distribute the impurities more evenly across

the grain boundaries but the weakening effect is not sufficiently enough to induce a change in the crack propagation behavior (i.e. transgranular vs. intergranular fracture) [26].

Cold-Rolling, HPT and ECAP are all top-down methods, methods of bottom-up such as a powder-metallurgical routes where sub-micrometer tungsten powders are pressed in a die and heated under compression load have shown only limited success due to grain growth and a high porosity and need further improvement [27].

1.3.4 Laminated Composites

To transfer the superior mechanical properties of cold rolled tungsten foils to bulk materials it is necessary to produce laminated composites. Different combinations of tungsten foils and interlayer material have been investigated for instance W-AgCu, W-Cu, W-V and W-Pd [28]. For example, W-Cu laminates with 60% tungsten content showed excellent behavior with a tensile strength of about 900 MPa and an elongation at fracture of 15%. The W-AgCu laminates showed higher strength of 1300 MPa but lower elongation at fracture of about 3.5%. In Charpy impact tests the W-Cu laminates exhibited a DBTT of 220 °C but shifted to higher temperatures when the laminated material was annealed at higher temperatures. W-AgCu showed a DBT at 100 °C but also shifter towards higher temperatures after annealing. The conclusion of this study was that the mechanical properties are mainly governed by the mechanical behavior of the tungsten foils which is not fully understood to this point [28]. The main goal in future is to stabilize the beneficial microstructure of the tungsten foils as it deteriorates in the annealing process which mimics possible working conditions in the fusion reactor.

1.4 Fatigue Crack Growth of Tungsten

To the best knowledge of the author fatigue crack growth (FCG) investigations on technically pure tungsten or alloys have not been done so far. Neither are there any experiments done on laminated tungsten composites. The only FCG investigation performed on tungsten is a sintered and forged tungsten alloy (93%W rest Ni, Fe) [29]. But this alloy is not quite comparable because this is dual phase material with brittle phase (W) embedded in a ductile matrix (Ni, Fe). This type of alloy yields its existence from the need of high density alloys which have applications in medicine to absorb X-rays or as weights in automotive industry and aviation industry [2].

This lack of data was the motivation to tackle the FCG behavior of tungsten and write this master thesis as a distinctive fatigue loading would also occur in fusion reactors, especially in ITER.

2. Material and Experiments

2.1 Material

The material used in this work is commercial pure tungsten that was manufactured by Plansee SE, Reutte, Austria. The purity is guaranteed to be at least 99.97 wt%. A list of typical impurities values is given in Table 1. Due to its high melting point tungsten is produced via the powder metallurgical route. After the tungsten powder is reduced by hydrogen (H_2) it is sintered, hot rolled and then cold rolled. Note that the terms hot rolled refers to rolling temperatures above the recrystallization temperature and cold rolling to those below. Tungsten plates with different thickness values of 2 mm, 1 mm and 0.1 mm were investigated. The degree of working increases with decreasing thickness. The true strain φ can be calculated using:

$$\varphi = \ln\left(\frac{h_0}{h_1}\right) \tag{1}$$

where h_0 is the starting thickness and h_1 the end thickness. The exact degree of deformation and rolling temperatures are not provided by the manufacturer.

Table 1: Typical values for impurities in technically pure tungsten by Plansee SE

	Al	Cr	Cu	Fe	K	Mo	Ni	Si	C	H	N	O	Cd	Hg	Pb
µg/g	1	3	1	8	1	12	2	1	6	0	1	2	1	0	1

2.1 Sample Preparation

To investigate the fatigue crack growth behavior of the plates with 2 mm and 1 mm thickness compact tension (CT) samples where cut out, with dimensions of w≈5.4 mm and a≈1.2 mm. A notch was introduced by a diamond wire saw which was further sharpened to a radius of about 5-20 µm with a razor blade and a 1 µm diamond paste. After that the side faces of all samples were polished by hand using sandpaper of values up to 4000 in order to eliminate scratches and to make it possible to identify cracks in the light microscope. The next step was to create an open and sharp pre-crack which was done with a resonance testing machine (Rumul Russenberger+ Müller, Switzerland) under cyclic compression load with a load ratio of R=10. An initial stress intensity range was impinged on the sample and if after 30,000 load cycles no crack was visible on both sides of the sample the stress intensity range was increased. This

procedure was repeated until a pre-crack was formed on both sides. Usually a value of 30-40 MPam$^{1/2}$ was sufficient to initiate a pre-crack with a length of 5-20 μm.

Due to the buckling instability of the 0.1 mm material a different strategy was necessary to introduce a crack. So, for the 0.1 mm foils single edge notched tension (SENT) samples with dimensions of 9x60x0.1 mm^3 were chosen which were cut including a notch by wire erosion from a big sheet. This notch was then also sharpened with a razor blade and 1 μm diamond paste to a radius of about 5-20 μm. As it is almost impossible to mechanically induce a pre-crack to such a thin foil, pre-cracking was done using a focused ion beam workstaion(FIB, Leo 1540, Zeiss) to cut a fine notch. The notch was cut with 10 nA for about 60-70 min and had a length of about 10 μm, Figure 4.

10 μm
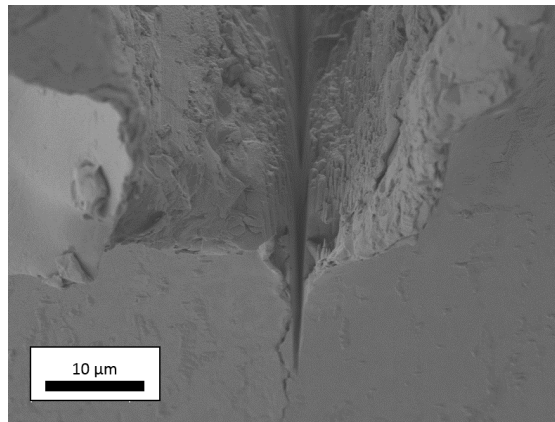
Figure 4: FIB-notched SENT sample

Since the cold rolling process induces a strong anisotropic texture in the tungsten foil (crystallographic as well as grain shape), it is important to investigate its influences on the FCG behavior. Therefore, samples from all strains with two different orientations were cut: T-L denotes samples where the crack propagates parallel to the rolling direction, whereas L-T denotes samples where the crack propagates perpendicular to the rolling direction, see Figure 5. The first letter in this denomination indicates the normal vector of the crack plane and the second letter the crack growth direction. For the 0.1 mm foil one additional orientation at an angle of 45° between these two orientations was prepared and is denoted as 45.

2.3 Experiments and Methods

The fatigue crack growth experiments were performed on an Instron E3000 electrodynamic testing system with a 250 N load cell and a sinusoidal force with typical frequencies between 20 Hz and 45 Hz and load ratios of R=0.1 and R=0.7. To gain knowledge on the frequency dependency (or in other words loading rate) additional experiments were carried out with 1 Hz and 0.1 Hz. To find the stress intensity threshold ΔK_{th} the load rising method was used. First the specimen is loaded with a stress intensity of about 3-5

MPam$^{1/2}$, where no crack propagation is expected for tungsten. If after 200,000 cycles the crack length did not change more than 2 μm the stress intensity was increased by 0.3 MPam$^{1/2}$ and later when the stress intensity range was in the region of about 12 MPam$^{1/2}$ the steps were increased to 0.5 MPam$^{1/2}$. This procedure was repeated until the crack growth rates exceeded a level of $2*10^{-11}$ m/cycle and propagated until final failure. It has also to be noted that during each step of the load rising method the force amplitude was held at a constant level and the increase of the stress intensity range was due to extension of the crack length a and the geometry factor. The stress intensity range ΔK and the geometry factor Y(a/W) was calculated using:

$$\Delta K = \frac{\Delta F \cdot Y\left(\frac{a}{W}\right)}{\sqrt{1000 \cdot B \cdot \sqrt{W}}} \tag{2}$$

with $$Y\left(\frac{a}{W}\right) = \frac{\left(2+\frac{a}{W}\right) \cdot \left(0.886 + 4.64 \cdot \left(\frac{a}{W}\right) - 13.32 \cdot \left(\frac{a}{W}\right)^2 + 14.72 \cdot \left(\frac{a}{W}\right)^3 - 5.6 \cdot \left(\frac{a}{W}\right)^4\right)}{1 - \left(\frac{a}{W}\right)^{3/2}} \tag{3}$$

and $Y\left(\frac{a}{W}\right) = 1.935 \cdot \left(\frac{a}{W}\right)^{1/2} + 4.124 \cdot \left(\frac{a}{W}\right)^2 + 3.227 \cdot \left(\frac{a}{W}\right)^5 - 4.425 \cdot \left(\frac{a}{W}\right)^{10} + 6.685 \cdot \left(\frac{a}{W}\right)^{20} + 12.22 \cdot \left(\frac{a}{W}\right)^{100}$ (4)

In equation 2 ΔF denotes the force range, a the crack length, W the width of the specimen and B the thickness of the specimen. The equation 3 relates to the geometry factor for CT-samples and originates from ASTM E399. Equation 4 relates to the SENT-samples used for the thin foils and was calculated with Matlab from a finite element simulation of the test setup carried out in Abaqus by Stanislav Zak. The difference to the normal SENT-configuration was that the clamps do not allow a rotation.

To measure the propagation of the crack during the FCG experiment the direct current potential drop (DCPD) technique was used. For this technique a constant electric current (here typically in the range of 2-3 A) is applied to the sample through spot-welded wires in the case of the CT samples and through the clamps for the SENT samples. With two additional wires, spot-welded symmetrical around the notch, the
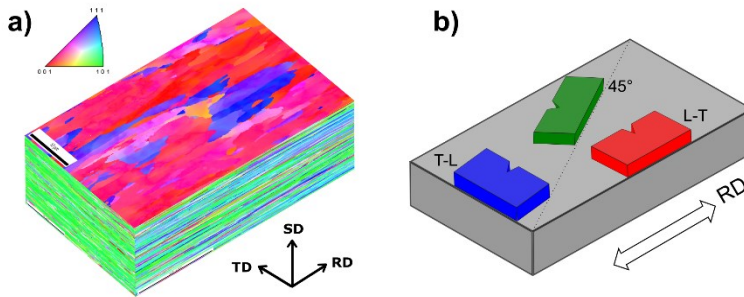

Figure 5: a) Inverse pole figure of the 0.1 mm tungsten foil showing the strong anisotropic texture. b) Sample orientation within the cold rolled sheet [Figures used with permission of Vladica Nikolic]

potential drop due to the current is measured with a nanovoltmeter (Keithley 2182A). The setup can be seen in Figure 6.

Analysis of the fracture surfaces after the FCG tests were done with a scanning electron microscope (SEM, Leo Gemini 1525) with a field emission cathode in combination with a secondary electron (SE) detector. For microstructure investigations an electron back scatter (BSE) detector from Bruker was utilized.

The hardness of the materials was measured with a Vickers hardness test with a load of 0.1 kg in order to obtain an estimation on the yield strength. This was done by multiplying the hardness values by a factor of 3 using Tabor´s rule [30].
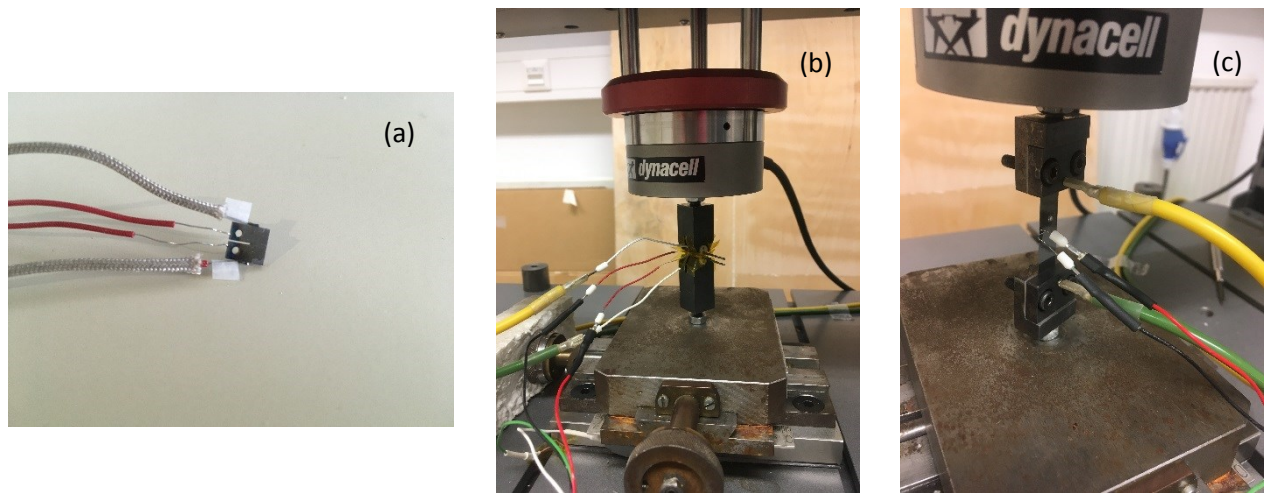
Figure 6: (a) a CT-specimen with spot-welded cables, the thinner red cables measure the potential drop while the thicker grey introduce the current (b) a CT-specimen installed into the testing machine (c) a SENT-specimen built into the testing machine, here the current is introduced through the clamps that hold the specimen.

3. Results

3.1 Hardness measurements

The hardness of the 2 mm tungsten sheet was measured at 533 ±12 HV which is mean value from 10 measurements. Values for W 1 mm and W 100 μm are taken from literature [23]: 595 HV0.1 and 687 HV0.1.

3.2 Microstructure

In Figure 7 the Inverse Pole Figure (IPF) maps of the 2 mm material can be seen. These and all following scans where taken from samples with a TD principal direction (rolling direction is in horizontal direction). As the grains in RD and TD have mostly a {101} orientation and a {001} orientation in SD, a pronounced rotated-cube texture is prevailing. The grains show a distinctive elongation in RD and have a pancake-like shape with a grain size of about 1.2 μm in SD. This was measured using the line intersect method.
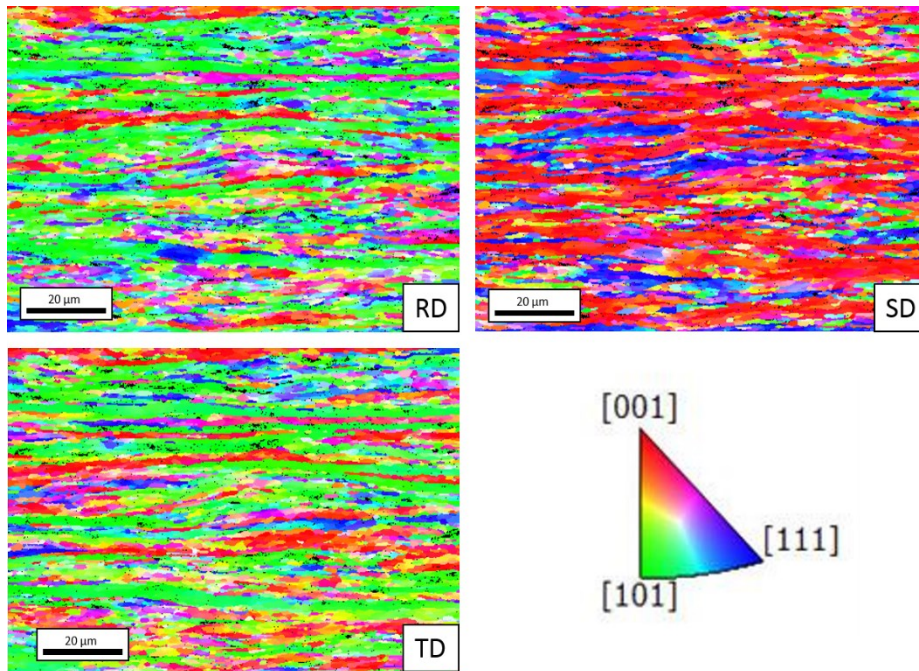
Figure 7: Inverse Pole Figure maps of W 2mm from the TD principal direction (rolling direction is horizontal)

Figure 9 depicts the IPF maps from W 1mm, again the rolling direction is horizontal. It is clearly visible that the grain size has decreased in SD direction to about 850 nm but the grains seem more elongated in RD, i.e. the pancake-like shape is more developed. Also the rotated cube corner texture is further evolved as the RD and TD viewing direction are more green, while SD is more red.
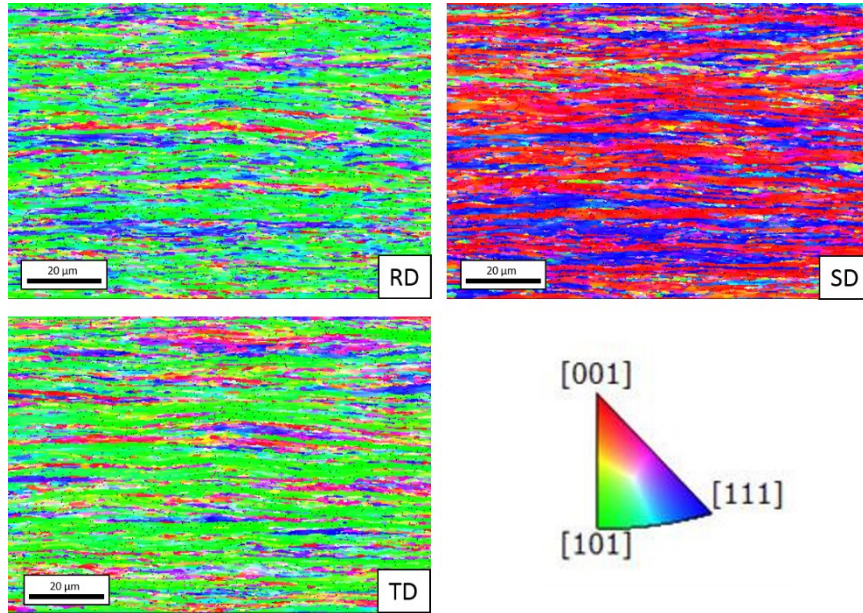
Figure 9: IPF maps of W 1 mm. The principal viewing direction is TD (rolling direction is horizontal)

Microstructural analysis of W 100 µm can be seen in Figure 8. The IPF maps also indicate rotated cube texture as before. This appears to be the saturation texture, which matches results from literature [21]. The grain size has decreased to about 180 nm when measuring in SD, which was again calculated using the line intercept method and counting only HAGBs.
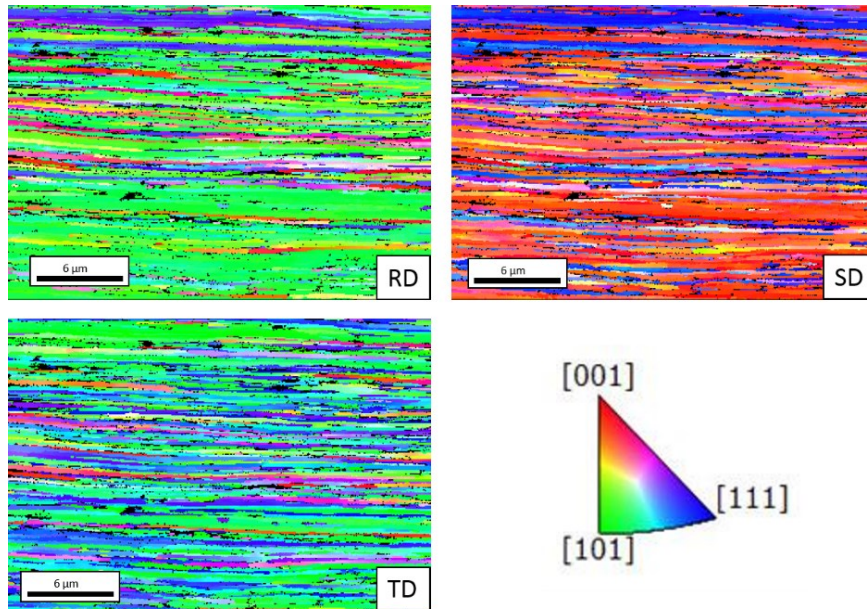

Figure 8: IPF maps of W 100 µm material in TD principal direction (rolling direction is horizontal).

All IPF maps were kindly created by Stefan Wurster and Daniel Firneis. Permission for use was granted.

3.3 FCG Results

In this section the results of the FCG-experiments will be presented. In the following diagrams open symbols indicate data from experiments with a load ratio of R=0.1 while filled symbols indicate data from R=0.7.

3.3.1 Tungsten 2 mm

In Figure 10 the results of the FCG-experiments performed on the 2 mm material can be seen. It is clearly visible that for both orientations the long crack threshold stress intensity factor ranges ΔK_{th} are considerable higher at lower load ratios. For the T-L orientation a ΔK_{th}=17.4 MPam$^{1/2}$ and ΔK_{th}=9.0 MPam$^{1/2}$ was found, for R=0.1 and R=0.7 respectively. The L-T orientated specimen showed considerably higher values of ΔK_{th}=21.1 MPam$^{1/2}$ and ΔK_{th}=10.7 MPam$^{1/2}$, for R=0.1 and R=0.7 respectively. All specimens ultimately failed before the crack propagation would reach the Paris-regime. So no evaluation of the Paris-exponent and therefore conclusions on the crack propagation mechanisms can be derived from the FCG-diagrams.
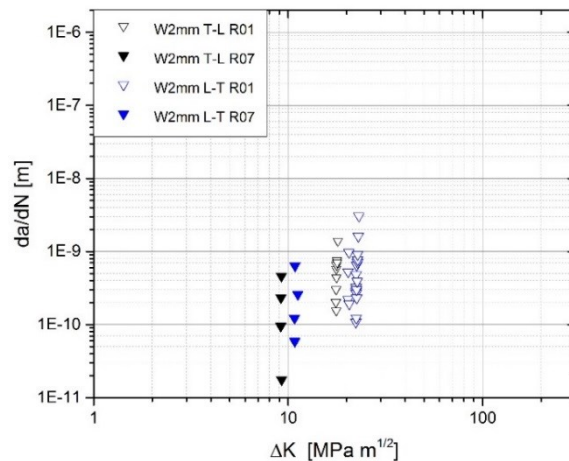
Figure 10: FCG-curves, da/dN vs ΔK, of 2mm sheets

3.3.2 Tungsten 1 mm

The results for the 1 mm thick material are depicted in Figure 11. Here the situation is very similar to the 2 mm material. The L-T is the stronger orientation where threshold stress intensity factor ranges of ΔK_{th}=22.1 MPam$^{1/2}$ and ΔK_{th}=10.5 MPam$^{1/2}$ were measured, for R=0.1 and R=0.7 respectively. Specimens with a T-L orientation again exhibited distinctively lower values although the influence of the load ratio seems to be smaller as the difference in the long crack threshold is smaller (ΔK_{th}=14.6 MPam$^{1/2}$ and ΔK_{th}=9.4 MPam$^{1/2}$, for R=0.1 and R=0.7 respectively). Similarly, as with the 2 mm samples, all 1 mm specimens ultimately failed before the crack propagation reached the Paris-regime. However, the cracks

propagated for somewhat longer and started to "bend" into the Paris-regime. So again no conclusion on the mechanisms of crack propagation can be made based on measuring the slope of the curve in the Paris-regime.
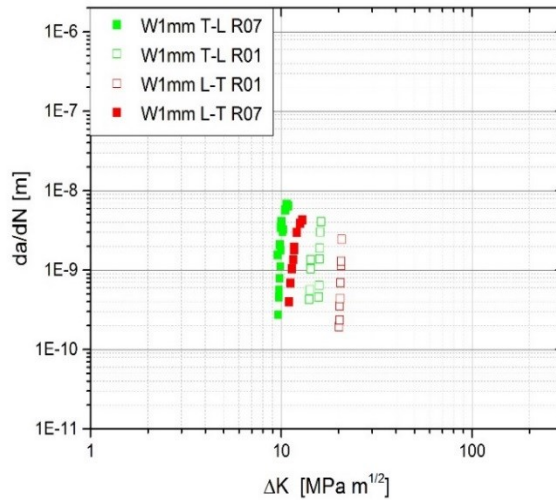

Figure 11: FCG-curves, da/dN vs ΔK, of 1 mm sheets

3.3.3 Tungsten 100 µm

A different picture yield the FCG experiments on the foils with 100 µm thickness, as seen in Figure 12. In all three directions (T-L, L-T and 45°) the crack propagated for several millimeters at the last load level so the FCG-curves show a distinctive Paris-regime. An evaluation of this regime will be given in the next section. As with the other two thicknesses there is a strong dependence of the threshold stress intensity factor ranges ΔK_{th} with the load ratio, i.e. ΔK_{th} values are significantly higher at R=0.1 than for R=0.7 (a summary for the values is given in Table 2 in the next section). Also there is an anisotropy of the FCG behavior. However, in contrast to the other material states the T-L orientation for the foils seems to be the stronger orientation (i.e. ΔK_{th} values of the T-L are higher for both load ratios than for L-T). Specimens oriented with 45° have the highest values for ΔK_{th}. Looking at the diagrams it is noticeable that the da/dN-rates at R=0.7 are higher by a factor of approximately 2-3 for all three orientations than at R=0.1. In Figure 12d all three orientations are plotted together to give a better comparison. Here the L-T specimens are the strongest, with the lowest da/dN-rates while T-L specimens exhibit the highest da/dN-rates. Rates for 45° oriented specimens lie between those two.
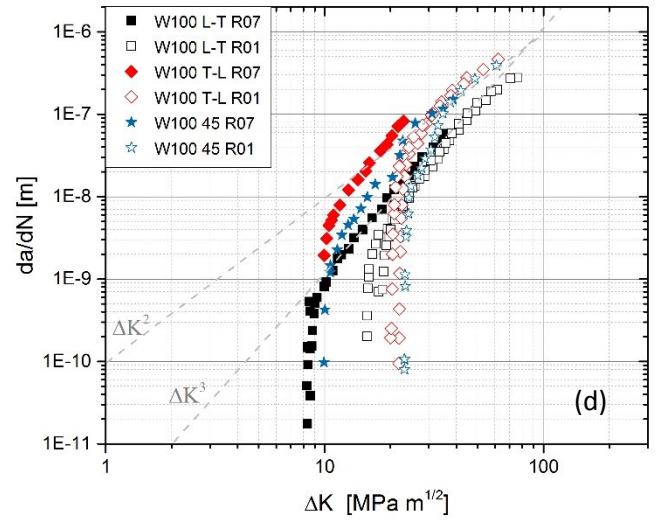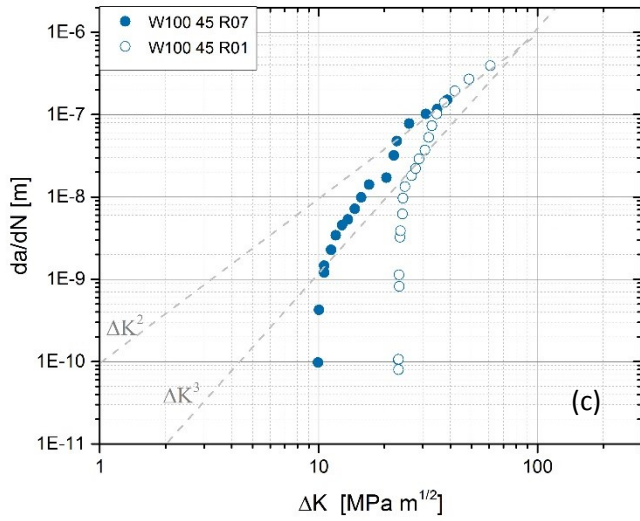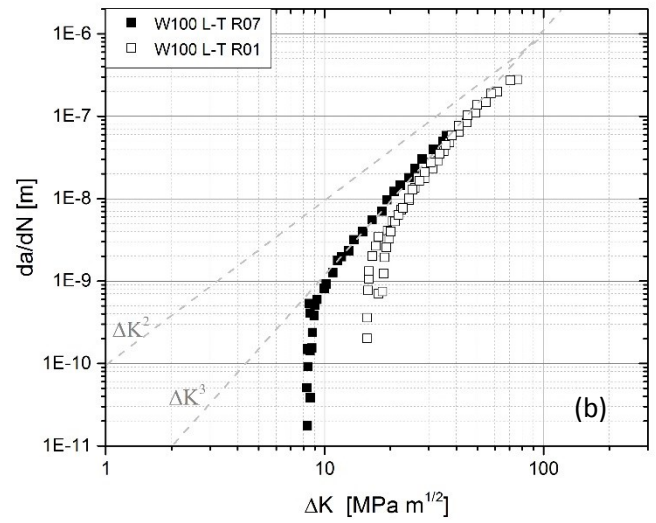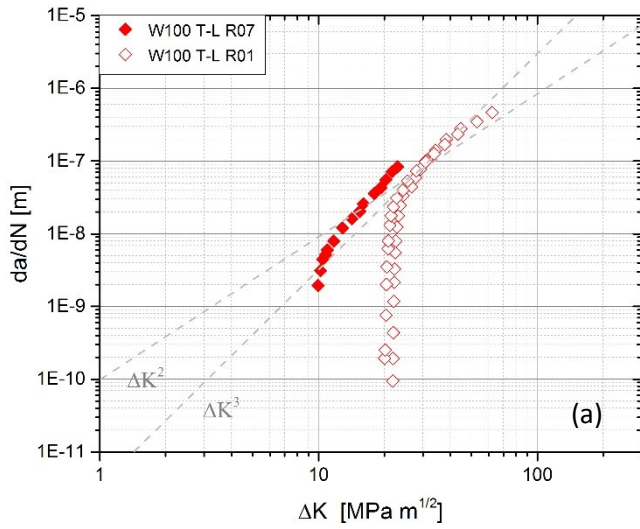
Figure 12: FCG diagrams from the 100 µm tungsten foils with (a) T-L, (b) L-T and (c) 45° orientation. In (d) all curves are depicted in one diagram for a better comparison. In all diagrams two gray dotted lines are depicted which represent slopes of 2 and 3 in the Paris-regime.

3.3.4 Low Frequency Experiments

One specimen of the W 100 μm material with T-L orientation was tested with varying frequencies. The test started as the others with the load rising method, although an accelerated procedure was carried out with increased load steps (i.e. ΔK was raised by 1 MPam$^{1/2}$ at each step). In Figure 13 the results can be seen. At first it seems astonishing that ΔK_{th} is much lower at around 13.5 MPam$^{1/2}$ than for the standard test (depicted in open gray symbols in Figure 13), but since the step size was significantly increased there was a shorter amount of time for oxidation of the fracture surfaces and hence less crack closure. A more detailed explanation of the effect of oxidation will be given in section 4. After the threshold was reached the frequency was reduced to 1 Hz and the crack was allowed to extend for about 600 μm before the frequency was further reduced to 0.1 Hz. With this frequency the crack propagated until final failure of the specimen. These results are depicted in blue for 1 Hz and green for 0.1 Hz. Since there was a time gap of about one day when switching the testing frequency oxidation could build up on the fracture surfaces and therefore da/dN-rates drop to lower levels and the crack had to accelerate again. When evaluating the data da/dN-rates seem to increase slightly when switching from 20 Hz to 1 Hz. After the switch to 0.1 Hz da/dN-rates increased by a factor of about 2-3, if data from 20 Hz is extrapolated to higher ΔK.
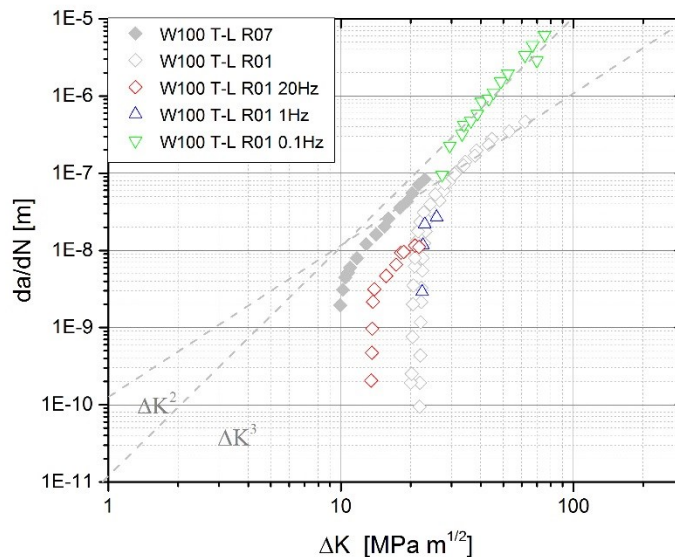

Figure 13: FCG-data from tests with lowered testing frequencies. Red symbols indicate 20 Hz, blue 1 Hz and green 0.1 Hz. Data from the standard tests are depicted in gray for comparison

3.3.5 R-Curves

From FCG-experiments employing the load rising methods, as it was used in this work, it is possible to generate R-curves that describe the rising crack growth resistance R with increasing crack length. When the crack starts to propagate at a certain ΔK it can come to a stop when the fatigue crack growth resistance

rises accordingly and equals the crack driving force K. Only when ΔK is increased the crack starts to grow and stops again when this equilibrium is established again. This is repeated until the specimen ultimately fails. The R-curve is generated when this ΔK is plotted against the crack extension. The results for the different materials and orientations are depicted in Figure 14. Like in the FCG-diagrams above open symbols indicate data from R=0.1 while filled symbols from R=0.7. As expected the curves evaluated at R=0.7 are much flatter as the difference of $\Delta K_{th,eff}$ and ΔK_{th} is smaller. R-values for the L-T orientation are generally higher than for T-L orientation. At R=0.1 specimens of all three materials show a sudden crack extension, marked with arrows in the diagrams. This is probably caused when the crack front hits favorable orientated grains for cleavage and can then propagate more easily. In general, the R-curves for the three materials have a similar appearance.
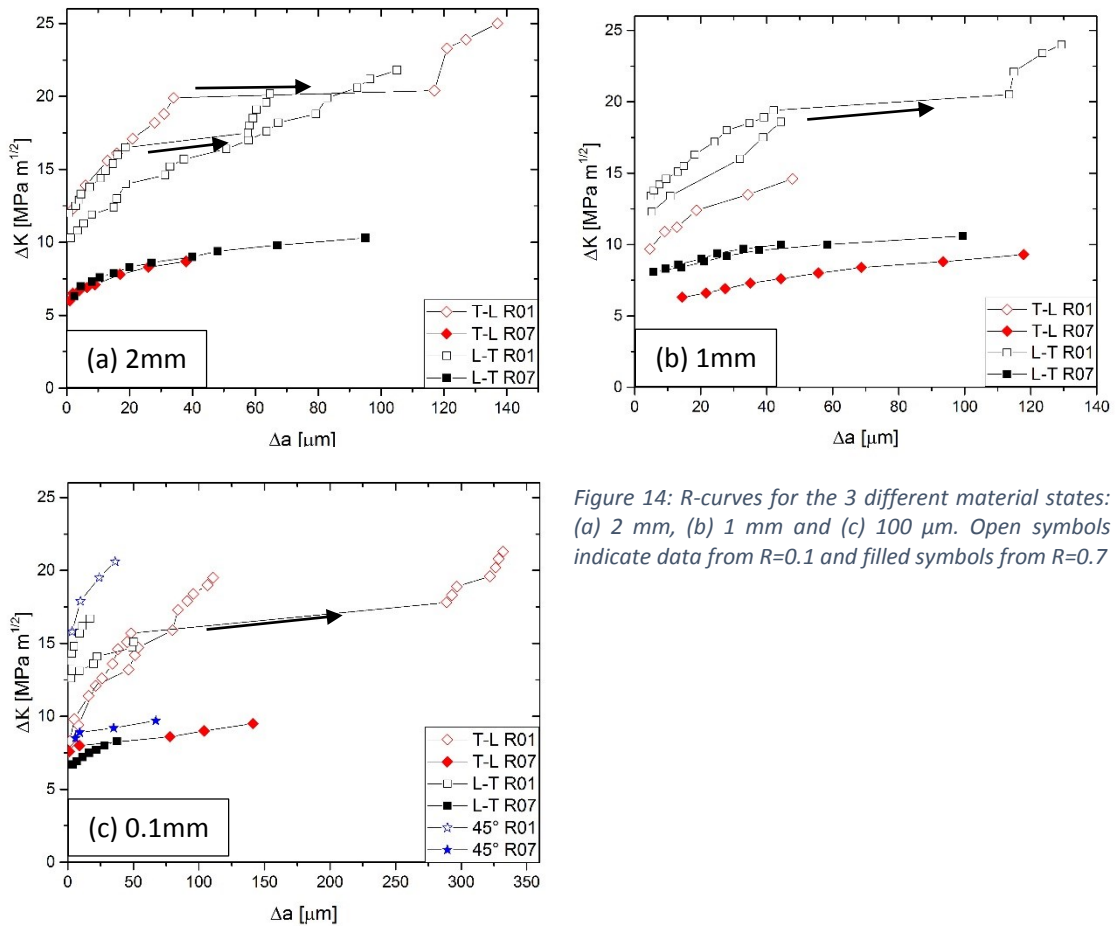

Figure 14: R-curves for the 3 different material states: (a) 2 mm, (b) 1 mm and (c) 100 µm. Open symbols indicate data from R=0.1 and filled symbols from R=0.7

21

3.3.6 Summary

In Table 2 a summary of all the threshold stress intensity factor ranges for all materials, orientations and load ratios are given. Due to the nature of the load rising method with discrete steps in the stress intensity factor range only a minimum value, the last step where the crack started to propagate and came to a stop, and a maximum value, where crack propagated until final failure of the specimen, for $\Delta K_{th,eff}$ and ΔK_{th} can be observed. To simplify the comparability a mean value was calculated:

$$\Delta K_{th,eff} = \frac{\Delta K_{th,eff}^{max} + \Delta K_{th,eff}^{min}}{2} \tag{5}$$

$$\Delta K_{th} = \frac{\Delta K_{th}^{max} + \Delta K_{th}^{min}}{2} \tag{6}$$

Some of the experiments were executed multiple times, so the depicted values in Table 2 are mean values of those experiments. In general $\Delta K_{th,eff}$, which is the stress intensity factor range where a first crack extension was measurable, is higher for R=0.1 than for R=0.7. Since $\Delta K_{th,eff}$ deviates strongly from ΔK_{th} for all specimens a cyclic R-curve behavior is present for all material states and orientations.

All three materials show a dependence on the mean stress intensity factor, i.e. the load ratio R, for ΔK_{th}. Also an anisotropic tendency is observable where the T-L orientation yields higher values than the L-T, for both load ratios. This seems to be reversed for the 100 µm material. There the 45° orientation exhibits the highest values. Although a clear tendency of the influence of increasing degree of deformation on ΔK_{th} is not possible to conclude from this data.

Table 2: Summary of all threshold stress intensity range values

		2 mm		1 mm		0.1 mm		
		T-L	L-T	T-L	L-T	T-L	L-T	45°
R=0.1	$\Delta K_{th,eff}$	10.5	10.9	8.9	12.6	7.1	13.0	15.6
	ΔK_{th}	17.4	21.1	14.6	22.1	20.7	16.4	23.0
R=0.7	$\Delta K_{th,eff}$	5.9	4.7	5.8	7.9	7.4	6.5	8.4
	ΔK_{th}	9.0	10.7	9.4	10.5	9.7	8.5	9.9

As mentioned above FCG experiments of the 100 µm foils exhibited a pronounced Paris-regime. In this regime a relationship between da/dN and ΔK can be described with a semi-empirical relation:

$$\frac{da}{dN} = C \cdot \Delta K^m \tag{7}$$

where C and m are material constants. The variable, m, in this formula is often referred as Paris-exponent and characterizes the slope in the double logarithmic FCG-diagram. These material constants where determined by curve fitting and are given in Table 3. For T-L and L-T orientations the Paris-exponent m is higher for R=0.7 than for R=0.1. The 45° orientation shows a reversed tendency with a lower m for R=0.7 than for R=0.1.

Table 3: Scaling parameters of the Paris-regime from the FCG curves of the 100 µm foils

	R=0.1		R=0.7	
	C	m	C	m
T-L	5.2E-12	2.8	1.3E-13	3.5
45°	2.3E-12	3.0	1.2E-12	2.6
L-T	4.6E-12	2.6	1.8E-13	2.9

3.4 Fracture Surfaces

3.4.1 Tungsten 2 mm

In Figure 15, 16, 17 and 18 SEM-images of the fracture surfaces from 2 mm tungsten are presented. In all these images the crack propagated from bottom to top. In the top left images an overview of the fracture surfaces is given and distinctive areas can be determined: at the very bottom the razorblade sharpened notch is visible. This is followed by short pre-crack performed under cyclic compression loading. After that differences between the two loading ratios can be constituted: at R=0.1 the area where stabile crack growth predominated (i.e. crack growth between $\Delta K_{th,eff}$ and ΔK_{th}) shows heavily disrupted surfaces which seems to come from oxidation and fretting (see Figure 15c and e and Figure 17c and d). Then an area which will be referred to as near-threshold region comes. This is the last step in the FCG-experiment where the crack grew until the sample ultimately failed. At the lower load ratio this area shows distorted grains and slight delaminations which indicate plastic deformation (see Figure 15d and f). The fracture mode is mostly transcrystalline but sometimes intercrystalline fracture occurred as well. Following this region is the overload fracture surface which exhibits clear cleavage with distinctive river patterns, e.g. Figure 15b. At R=0.7 the fracture surfaces exhibit a somewhat different appearance. A distinction between stable crack growth and a near-threshold region cannot be given. The stable crack growth region is characterized by more heavily deformed grains and many evenly distributed secondary cracks, marked with green arrows Figure 16c and d. There also some oxidation can be found but at a lower area fraction, indicated with green

arrows in Figure 16d. In this region exclusively transcrystalline fracture is predominant. Overload fracture is again characterized by transcrystalline cleavage fracture (Figure 16b).

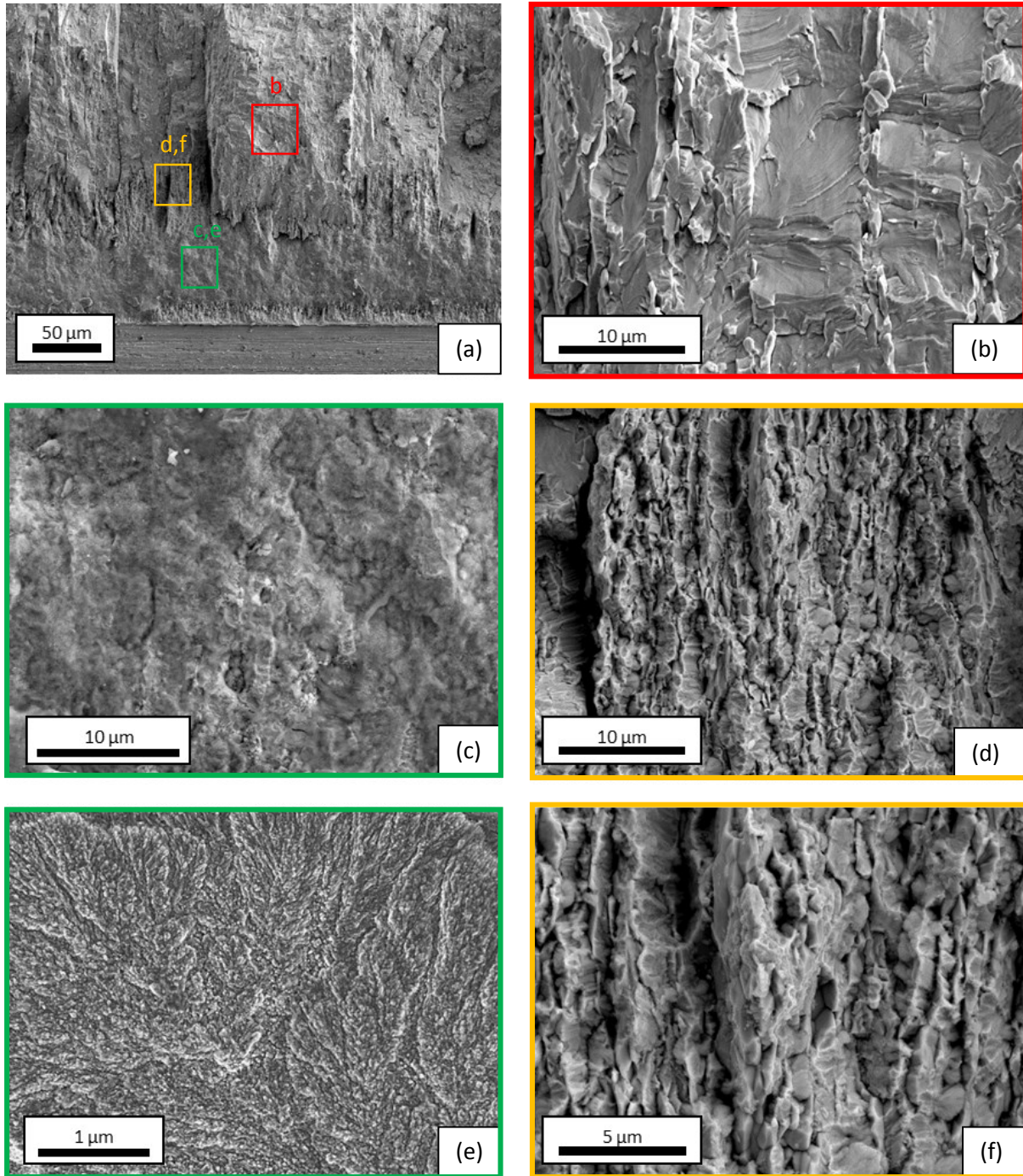Between the two orientations T-L and L-T no notable differences are observed.

Figure 15: SEM-fractographs of W 2mm T-L tested at R=0.1: (a) an overview, (b) overload fracture showing cleavage fracture, (c) and (e) oxidized surface from stabile crack growth, (d) and (f) details of the near-threshold region
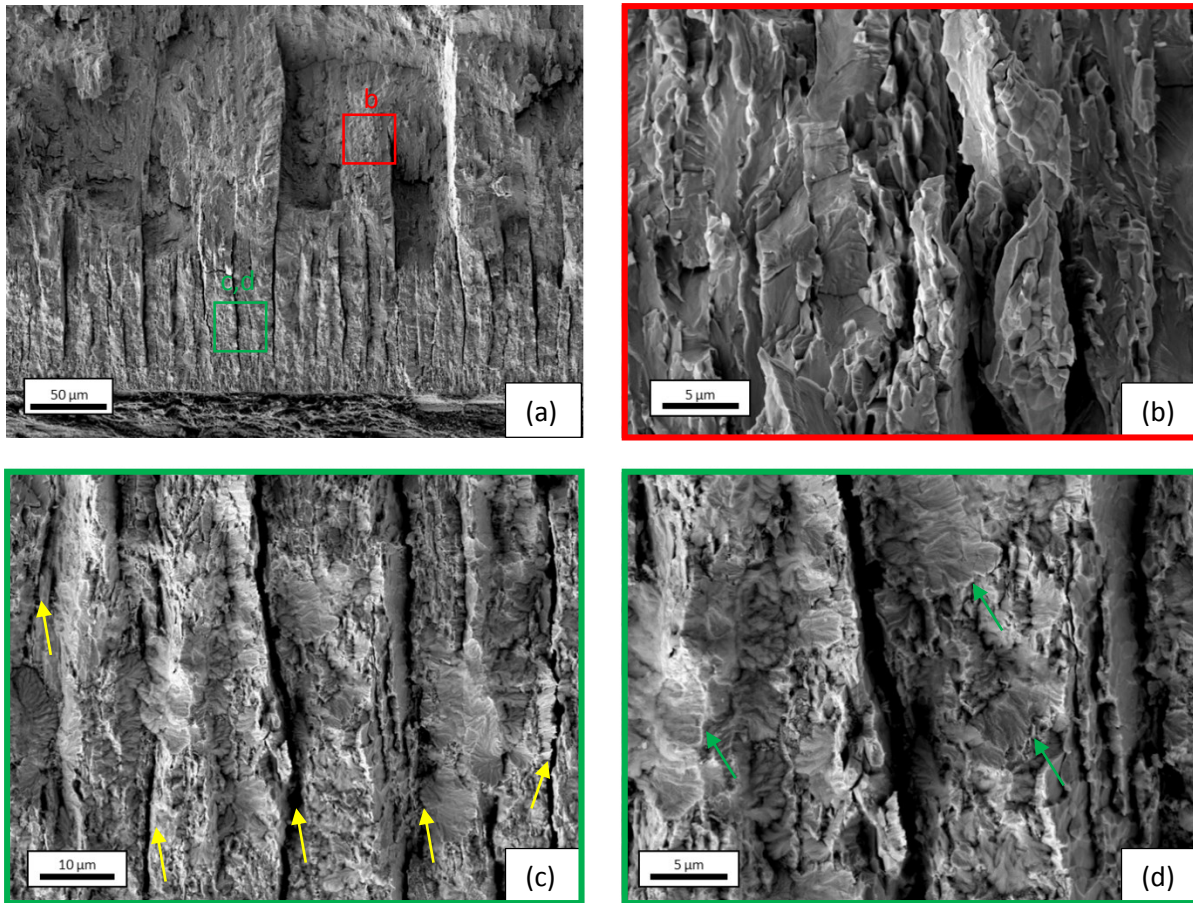
Figure 16: SEM-fractographs of W 2mm T-L tested at R=0.7: (a) Overview of the fracture surface, (b) detail of the overload fracture area showing cleavage, (c) and (d) details of the stable crack growth region: orange arrows mark secondary cracks while green arrows mark oxidized areas
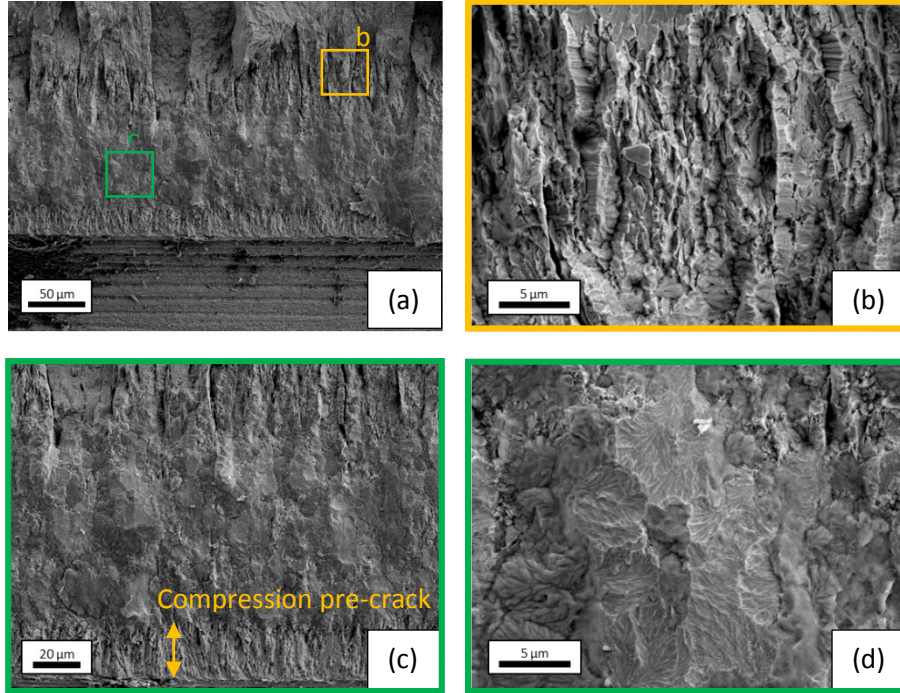
Figure 17: SEM-fractographs of W 2mm L-T tested at R=0.1 fracture surfaces: (a) an overview, (b) details of the near-threshold region, (c) and (d) oxidized surfaces where stable crack growth predominated
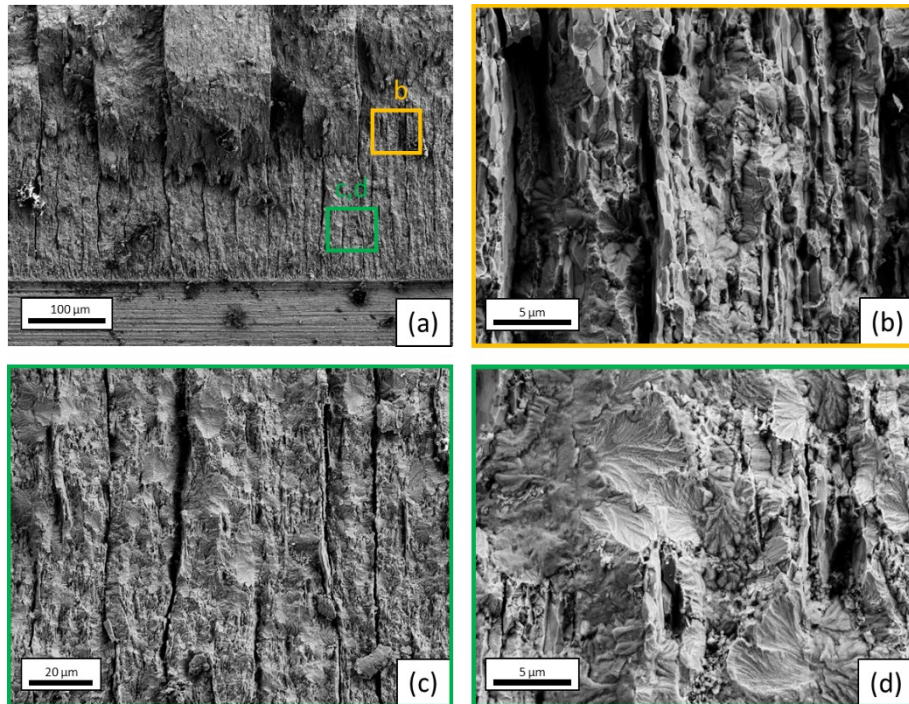

Figure 18: SEM-fractographs of W 2 mm T-L tested at R=0.7: (a) overview, (b) details of the transition area, (c) and (d) details of the near-threshold regime exhibiting secondary cracks and partial oxidation on the fracture surface

3.4.2 Tungsten 1 mm

As expected from the FCG-data, the fracture surfaces of the 1 mm material show a very similar behavior as the 2 mm material. After the compression pre-crack, the specimens tested at R=0.1 exhibits a heavily oxidized and therefore disrupted surface (e.g. Figure 19c and d, Figure 21c and d). In the near-threshold region slight necking and plastic deformation of grains is visible with some secondary cracks, as seen in Figure 19b and d and Figure 21b. Here a mixture of ductile trans- and intercrystalline fracture occurred. Although some grains exhibited a transcrystalline cleavage behavior, which can be found more towards the end of the near-threshold region and mark the transition to the residual fracture (ultimate failure). Again this final failure is distinguished by transcrystalline cleavage fracture but will not be shown in further figures as it is the same for all material states and loading directions. In contrast to the 2 mm samples specimens tested at R=0.7, the 1 mm specimens exhibit a different fracture pattern for stable crack growth and the near-threshold region (Figure 20a and Figure 22a) and can therefore be separated. Both of these regions show regularly distributed secondary cracking. In the stable crack growth region partial oxidation is observable (Figure 20c and e, Figure 22d and f), but it is seems to be slightly more than for the 2 mm material state. The unoxidized areas show strongly deformed grains and only transcrystalline fracture is present. In the following near-threshold region pronounced necking and beginning delamination is noticeable (Figure 20b and d and Figure 22c and e). The fracture mode is mainly transcrystalline, although some grain boundaries are visible and hence intercrystalline fracture was prevailing. Similarly, as the 2 mm material, the 1 mm material possesses only marginal differences between the T-L and L-T orientation. All 1 mm specimens showed a much longer crack extension (usually between 200 and 400 µm) during FCG-experiments than 2 mm specimens.
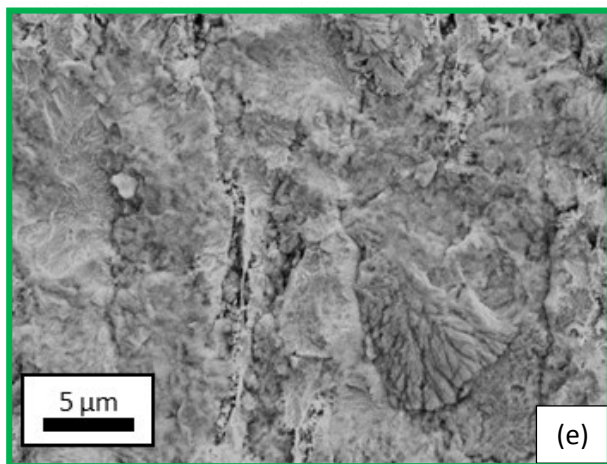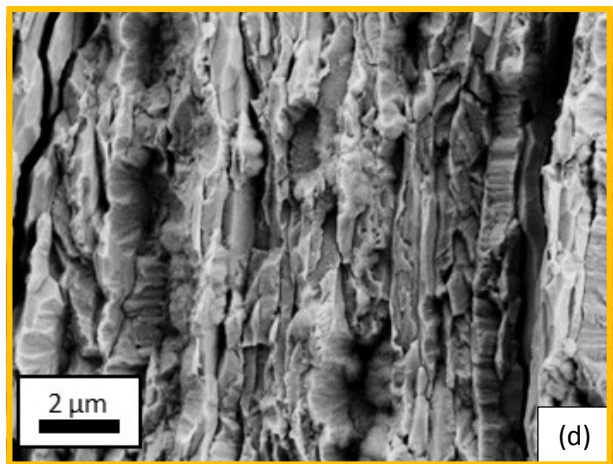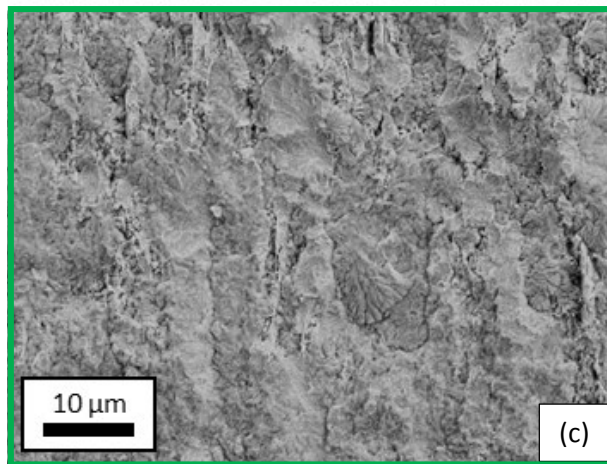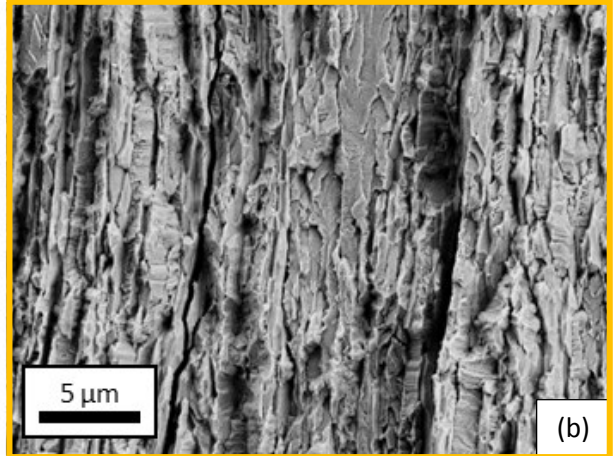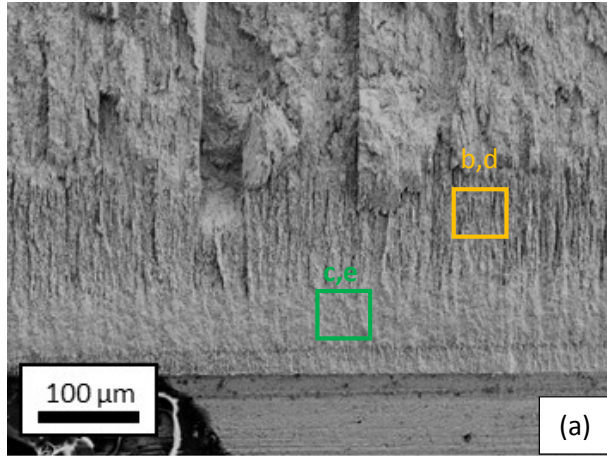
Figure 19: SEM-fractographs of W 1mm T-L tested at R=0.1: (a) overview, (b) and (d) near-threshold region exhibiting strongly deformed grains, (c) and (e) strong oxidation in the stable crack growth region
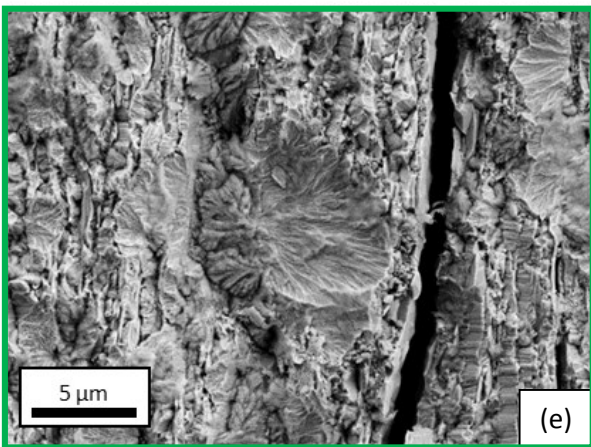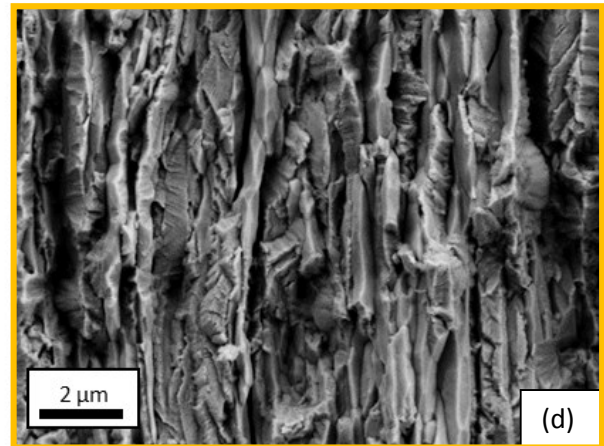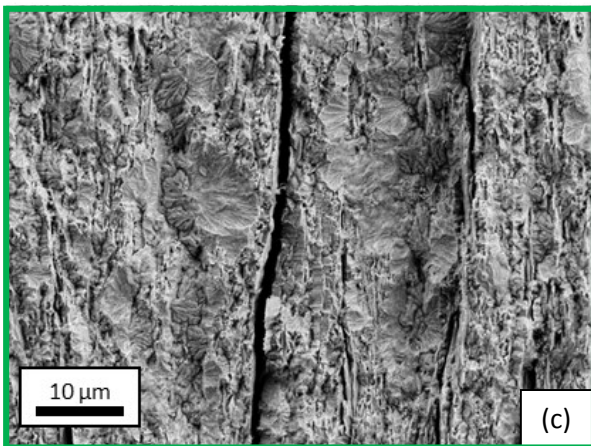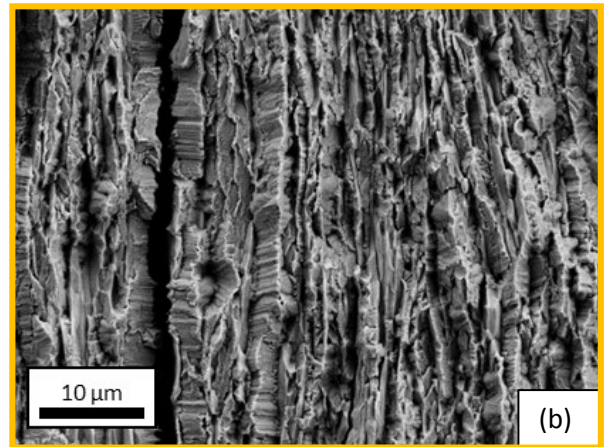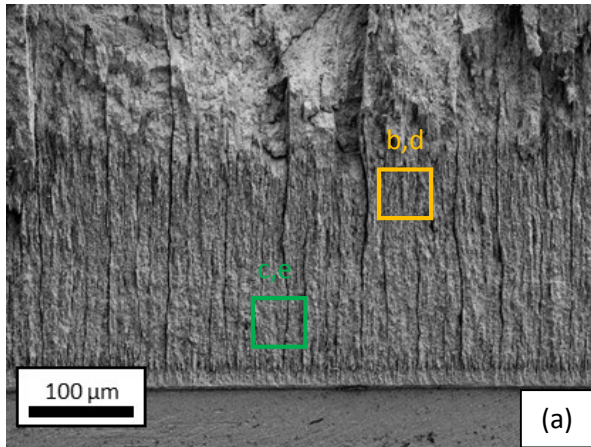
Figure 20: SEM-fractographs of W 1mm T-L tested at R=0.7: (a) overview, (b) and (d) near-threshold region with slightly delaminated grains exhibiting plastic deformation, (c) and (e) stable crack growth region with partially oxidized surface and secondary crack formation

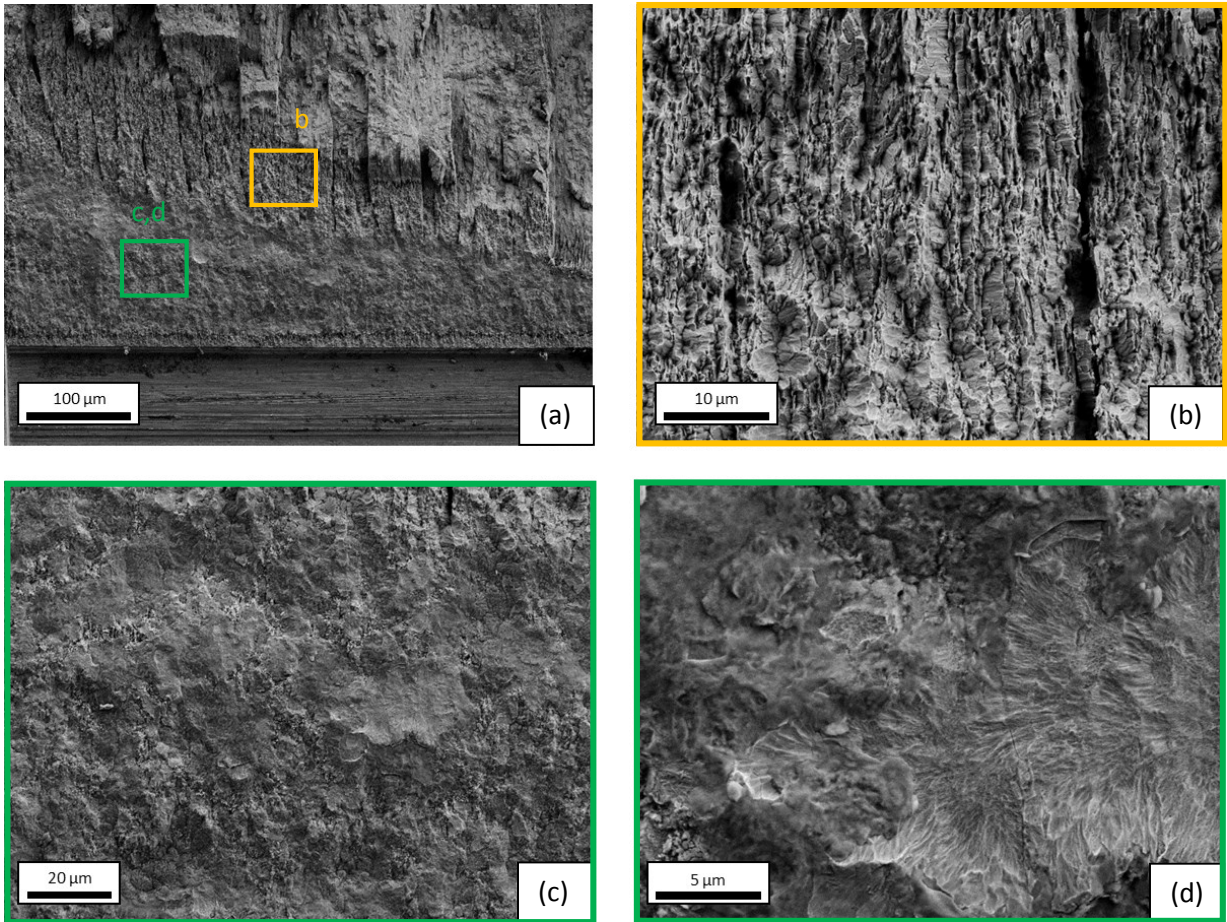*Figure 21: SEM-fractographs of W 1mm L-T tested at R=0.1: (a) overview, (b) near-threshold region, (c) and (d) heavily oxidized fracture surface from stable crack growth*
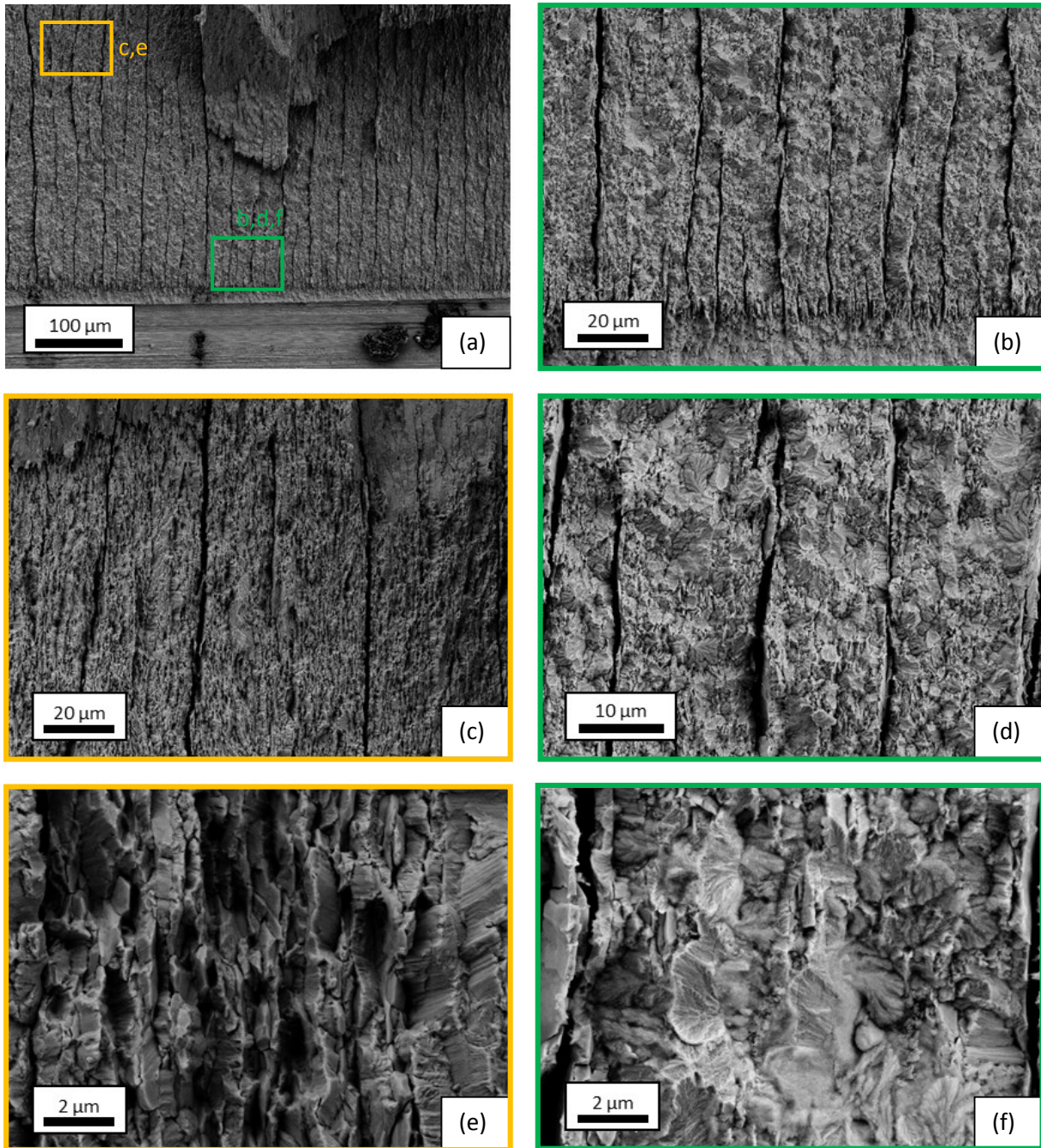
Figure 22: SEM-fractographs of W 1mm L-T tested at R=0.7: (a) overview, (b),(d) and (f) stable crack growth region with partially oxidized fracture surface, (c) and (e) near-threshold region showing mixture of trans- and intercrystalline fracture

3.4.3 Tungsten 100 μm

In this section the fracture surfaces of the 100 μm thick foils will be shown. In all figures the crack growth direction is from left to right. In Figure 23a an overview of the specimen with T-L orientation tested at R=0.1 can be seen. The first 200 μm of the crack extension shows some oxidation which can be linked to the R-curve regime of the threshold. In the following near-threshold region (depicted in Figure 23c and e) plastically deformed grains are visible and delaminations start to begin. At higher ΔK delaminations are more pronounced and the fracture surfaces appear less disrupted (Figure 23d and f). In Figure 23b the overload fracture is depicted which like the 2 mm and 1 mm material is characterized by cleavage fracture. At R=0.7 the fracture surface looks quite similar as at R=0.1 but again secondary cracks can be identified. At higher ΔK it appears that quasi-cleavage is emerging. Comparing T-L and L-T it stands out that the grain structure in L-T looks much smaller (Figure 25 and Figure 26) than in T-L. This is because in T-L the elongated grain axis lies parallel to the crack propagation direction, but when looking at the fracture surface of L-T specimens the viewing direction is in rolling direction and thus the grains look smaller. It is also interesting to note that the overload fracture in L-T specimens exhibit a more pronounced necking and hence a lot of plastic deformation with a wavy pattern (see Figure 25b, e and h and Figure 26b, e and h). It appears that plastic deformation in L-T specimens is more dominant, because no quasi-cleavage fracture pattern could be found, even at higher ΔK.

The fracture surfaces from specimens with 45° orientation can be seen in Figure 27 and Figure 28, for R=0.1 and R=0.7 respectively. Figure 27a presents an overview of the specimen, where two big cracks are noticeable. These probably come from damages from the electric discharge machining or razorblade polishing of the notch of the specimen. In the stable crack growth region (Figure 27c) strong oxidation is observable. In the Paris-regime also oxides can be seen with what looks like a shearing deformation. It is not clear whether this is a product of the FCG-experiment or it originates from poor handling of the specimen. At R=0.7 secondary cracks are observable and at higher magnifications the fracture pattern looks like a mixture of quasi-cleavage and intercrystalline fracture, although plastic deformation also seems to prevail.

The fracture surfaces from tests with varying test frequency are depicted in Figure 29 in low and high magnification. It is quite remarkable that the fracture patterns are almost identical although a jump in the da/dN-rates has been observed.
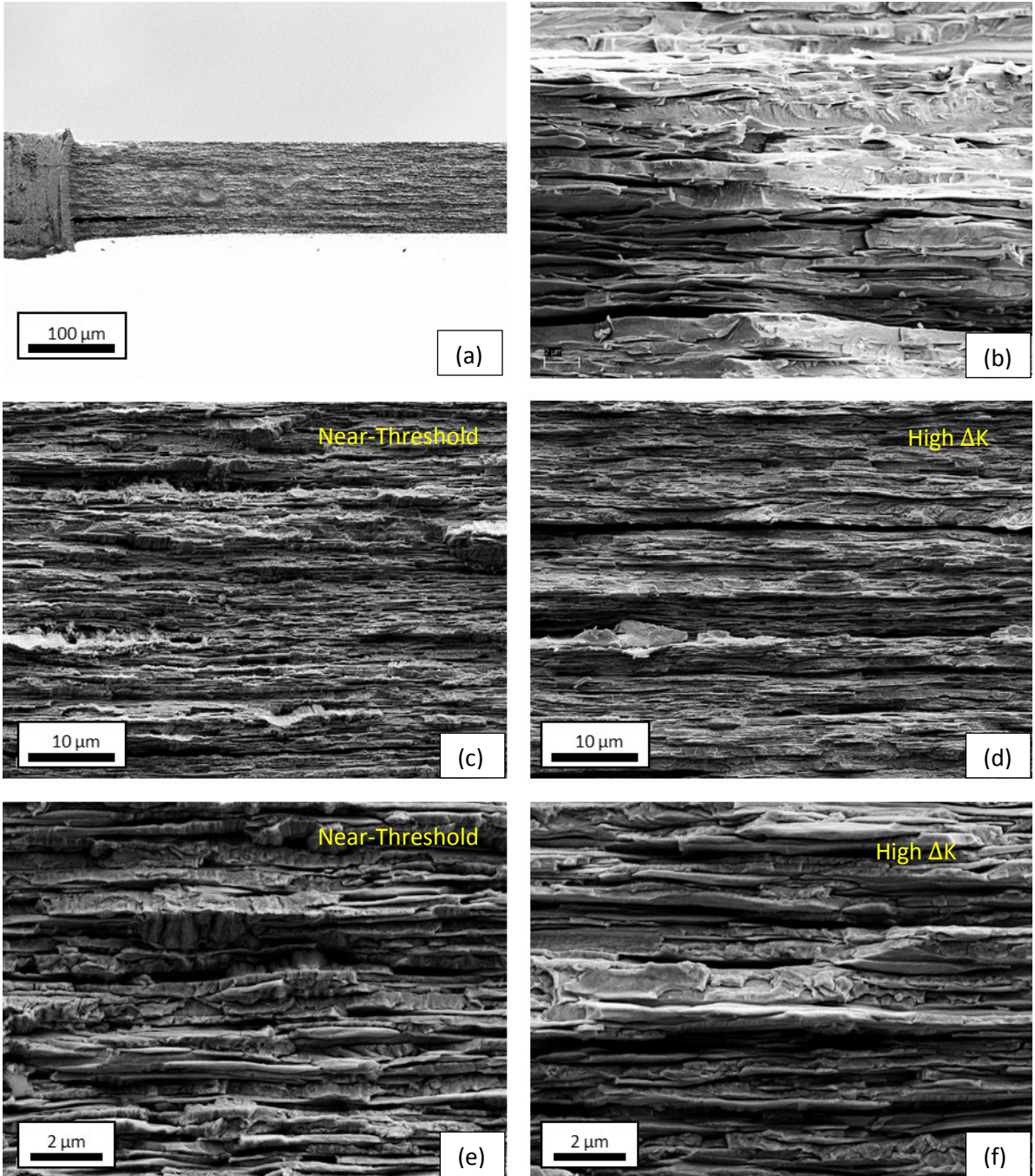
Figure 23: SEM-fractographs of W 100 µm T-L tested R=0.1: (a) overview of the fracture surface showing some oxidation for the first 200 µm, (c) and (e) near-threshold region, (d) and (f) close-ups at high ΔK

33
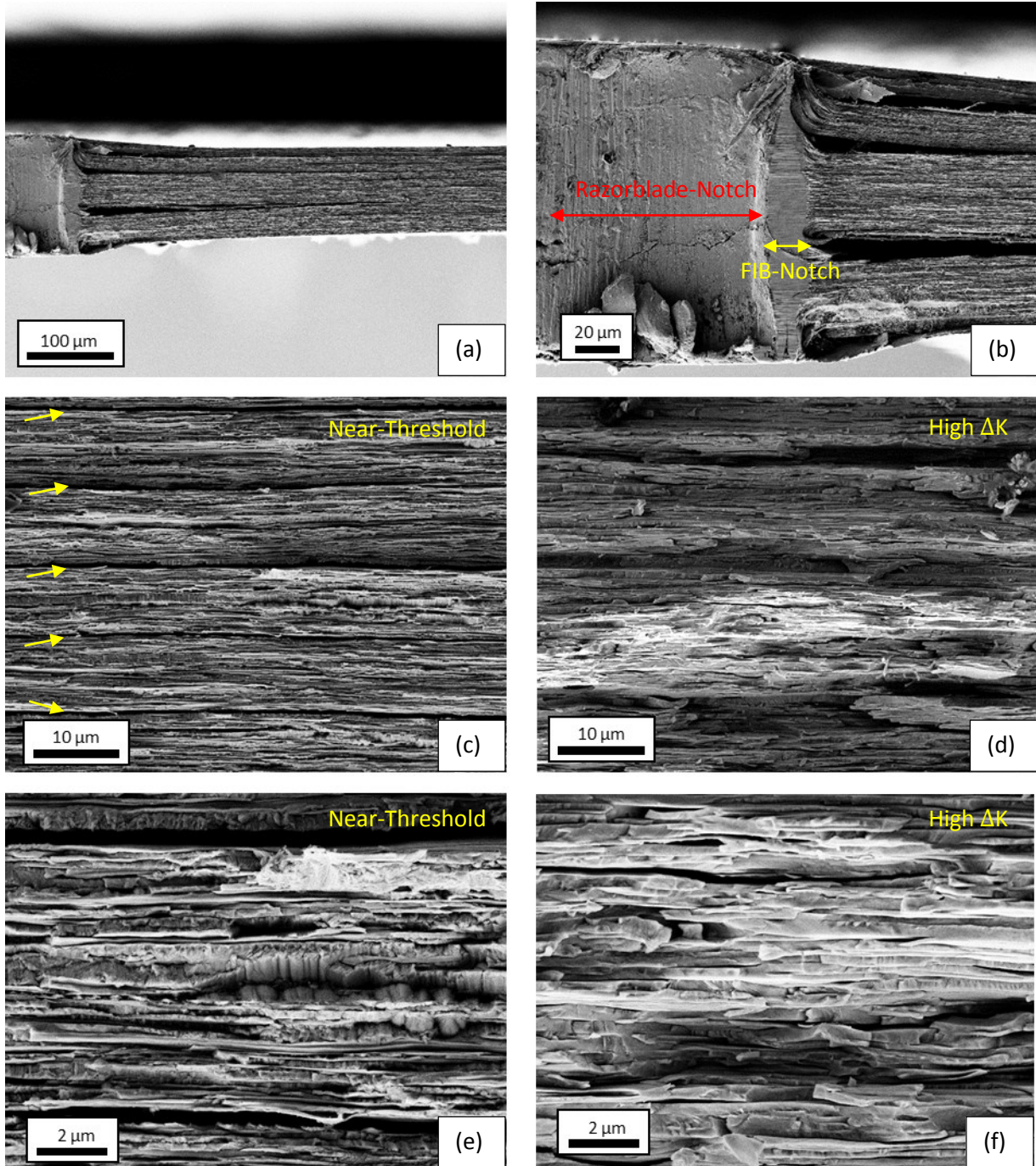
Figure 24: SEM-fractographs of W 100 µm T-L tested at R=0.7: (a) overview, (b) detail of the pre-crack cut with FIB, (c) and (e) details of the near-threshold region: secondary cracks which prevail mostly at R=0.7 are marked with yellow arrows, (d) and (f) details of fracture surfaces at higher ΔK
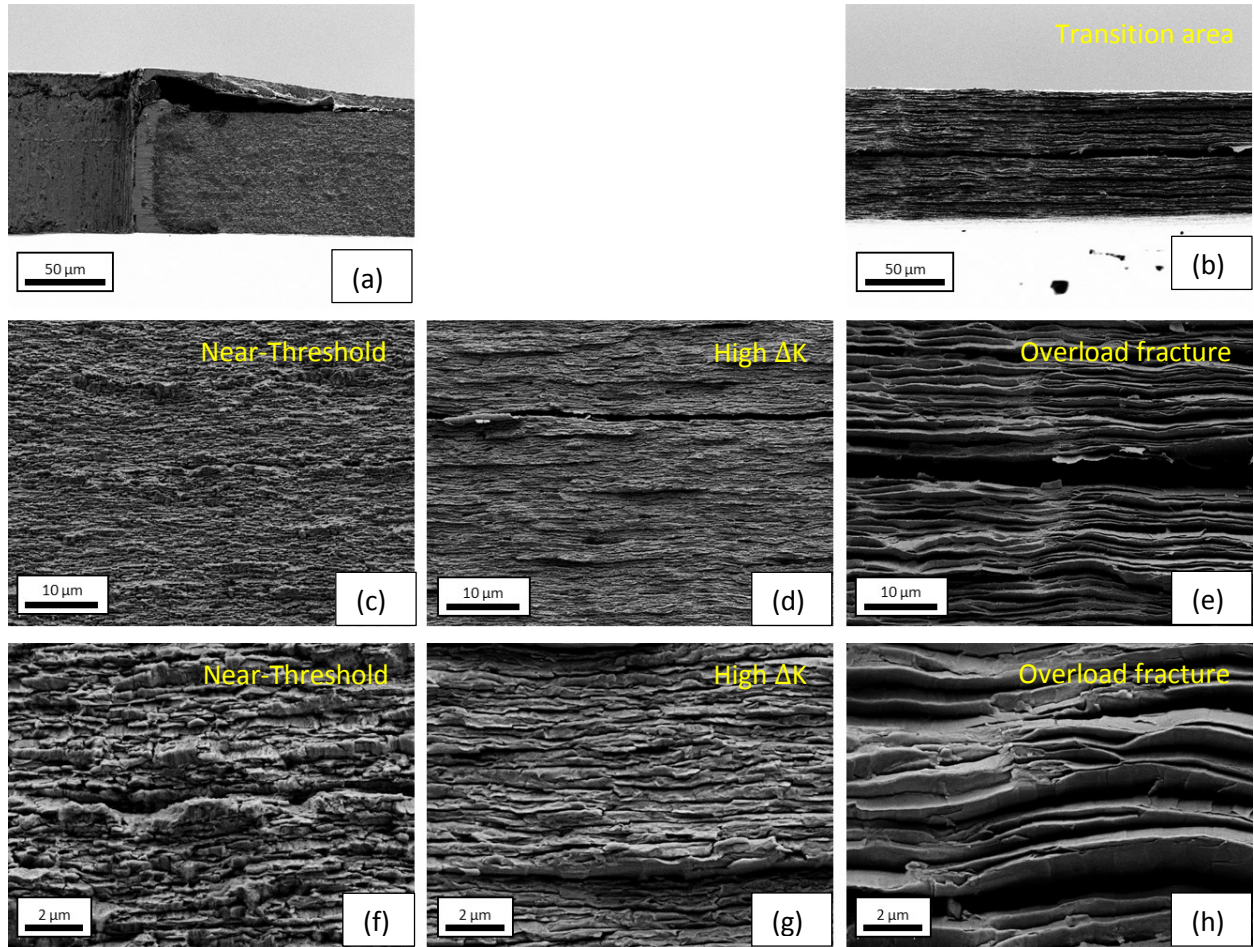
Figure 25: SEM-fractographs of W 100 µm L-T tested at R=0.1: (a) overview, (c) and (f) near-threshold region, (d) and (g) fracture surface at high ΔK, (b) (e) and (h) strong necking at overload fracture
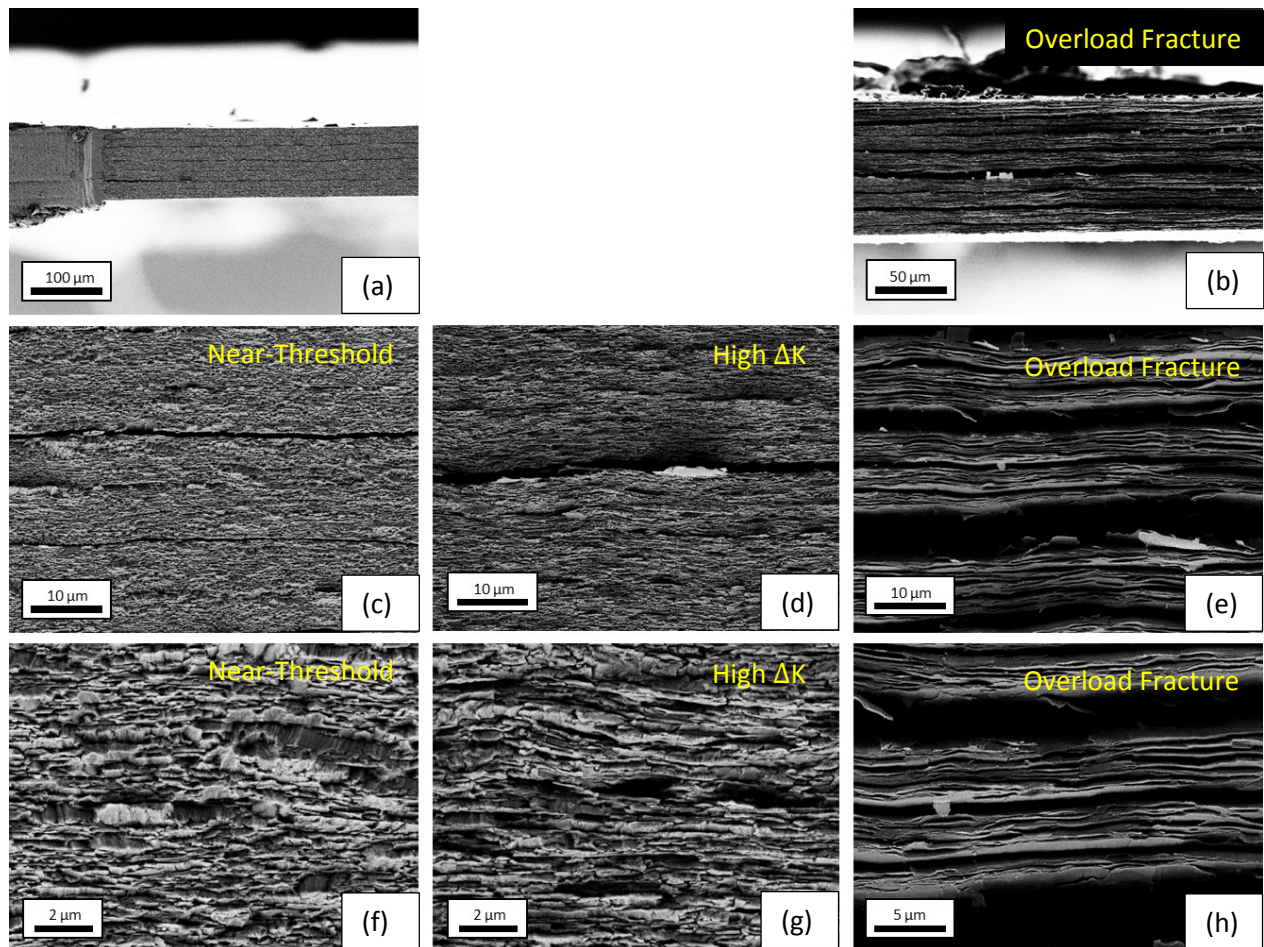
Figure 26: SEM-fractographs of W 100 µm L-T tested at R=0.7: (a) overview, (c) and (f) near-threshold region, (b),(e) and (h) overload fracture showing pronounced necking
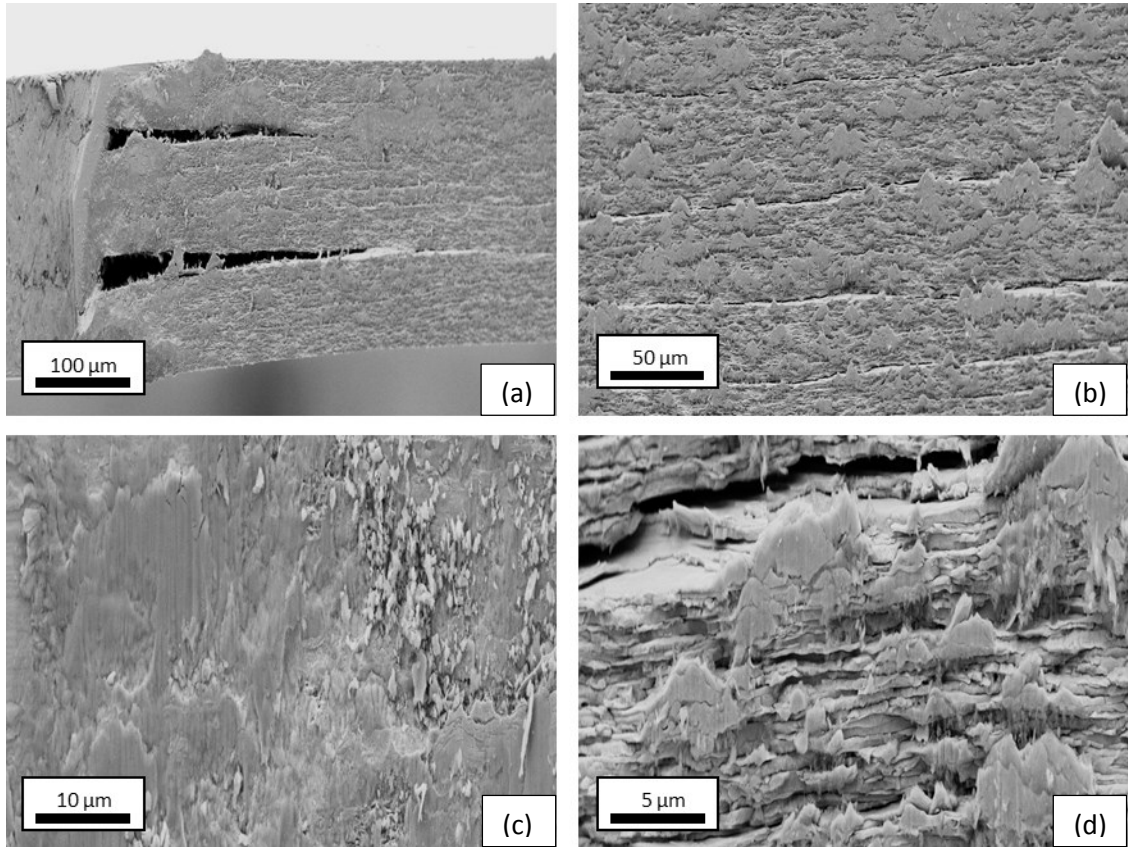
Figure 27: SEM-fractographs of W 100 µm 45° tested at R=0.1: (a) overview, (b) and (d) fracture surface in the Paris-regime: oxidation products are visible and show plastic deformation, (c) oxidation and fretting at stable crack growth
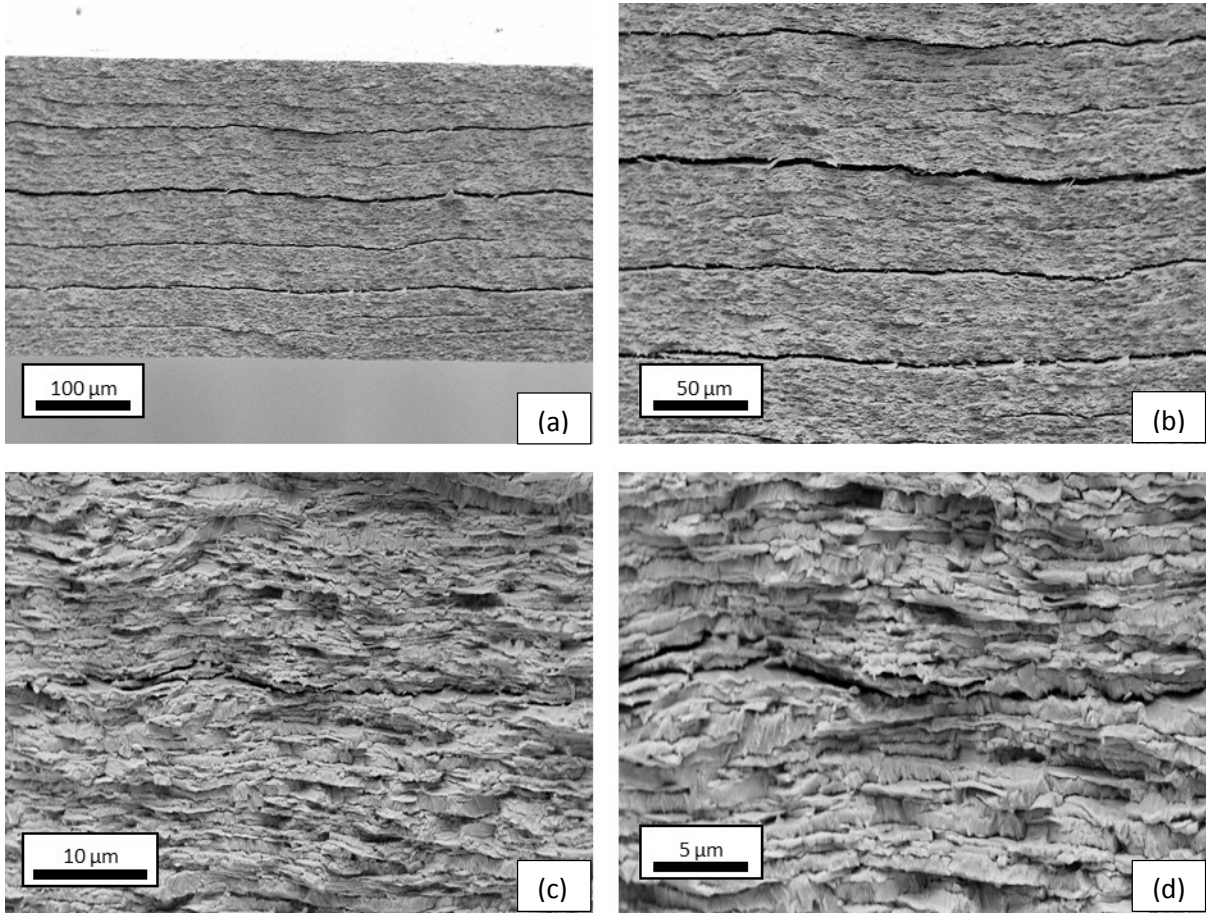
Figure 28: SEM-fractographs of W 100 µm 45° tested at R=0.7: (a) overview, (b), (c) and (d) fracture surfaces of the Paris-regime, secondary cracks are noticeable

20 Hz

1 Hz

0.1 Hz

Near-Threshold

Near-Threshold

High ΔK

High ΔK

50 µm (a)

5 µm (b)

50 µm (c)

5 µm (d)

50 µm (e)

5 µm (f)

50 µm (g)

5 µm (h)

Figure 29: SEM-Images of fracture surfaces at various frequencies: 20Hz, 1Hz, 0.1Hz

4. Discussion

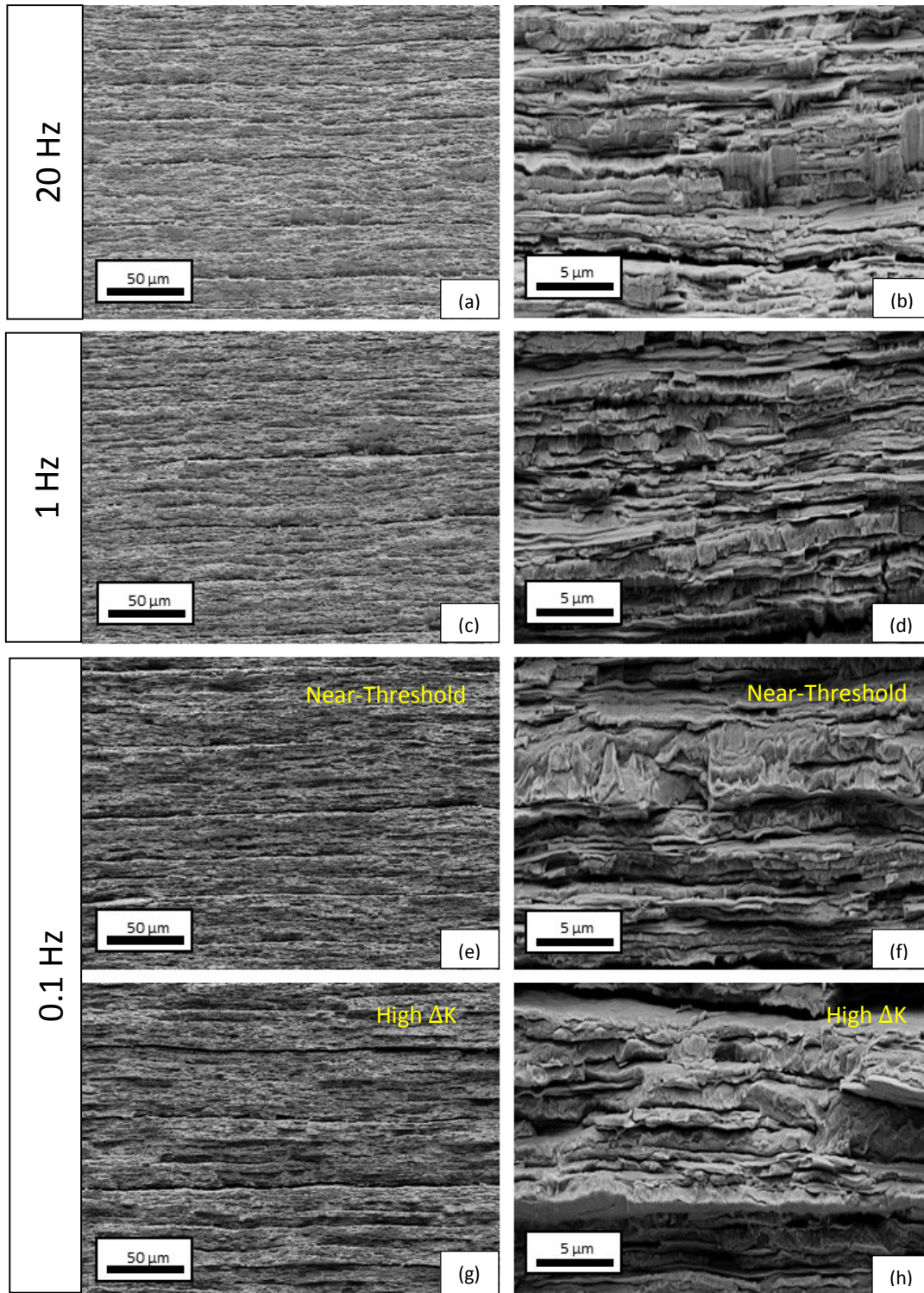Looking at the FCG-diagrams it is remarkable that the 100 μm foils exhibit a pronounced Paris-regime where the crack is extending for several millimeters. Both 2 mm and 1 mm materials only show a fatigue crack extension of about 150 μm to 400 μm and reveal no Paris-regime, although the crack extension of the 1 mm material is usually somewhat longer. In FCG experiments the specimen ultimately fail typically when K_{max} approaches the quasi-static fracture toughness K_{Ic}. K_{max} is dependent on ΔK and the load ratio and can be calculated by:

$$K_{max} = \frac{\Delta K}{1-R} \rightarrow K_{Ic} \tag{8}$$

So the higher degree of deformation seems to drastically improve K_{Ic} and hence high ΔK values can be reached leading to noticeable crack extension and a pronounced Paris-regime.

Although the fracture toughness for the severely deformed foils is significantly improved, the effect on the threshold stress intensity range ΔK_{th} seems to reach a saturation. In Table 2 it can be seen that further cold rolling from 2 mm to 0.1 mm does not induce significant changes of ΔK_{th} as they are roughly the same for all three materials.

4.1 Validity of the FCG-results

For the application of LEFM certain requirements have to be fulfilled. A crucial parameter for the validation is the size of the monotonic plastic zone r_{pl} which is calculated under plain strain conditions with:

$$r_{pl} = \frac{1}{3\pi}\left(\frac{K_I}{\sigma_y}\right)^2 \tag{9}$$

According to ASTM E399 the uncracked ligament (W-a) has to be larger than about 25 times the size of the plastic zone. The 2 mm and 1 mm specimens fulfill this requirement for all FCG-data points. The thin foils satisfy this requisition up to $\Delta K \cong 62$ MPam$^{1/2}$ and $\Delta K \cong 23$ MPam$^{1/2}$, for R=0.1 and R=0.7 respectively for all three orientations. Since the vast majority of FCG-data is under these limits it is assumed that conclusions that arise from the data are formally correct. A more severe limitation is the need for plain strain condition. Here the ASTM E399 requires for the thickness of the specimen to be about 25 times larger than the monotonic plastic zone. For the 2 mm material (thickness B~1.3 mm and σ_y=1600 MPa)

this also was fulfilled up to ΔK=31.9 MPam$^{1/2}$ and ΔK=10.6 MPam$^{1/2}$, for R=0.1 and R=0.7 respectively. Values for the 1 mm material were similar (B~1 mm, σ_y=1800 MPa) with ΔK=31.5 MPam$^{1/2}$ and ΔK=10.5 MPam$^{1/2}$, for R=0.1 and R=0.7, respectively. The thin 100 μm foils cannot fulfill these requirements of the standard. Even if they would fulfill them with their 100 μm thickness, it would be not for long since delaminations and secondary cracks divide the specimens into even thinner foils, amplifying the plain stress state that would start to prevail. Therefore, an evaluation of the criterion regarding a minimum specimen thickness is not meaningful for the microstructure as in the foils.

4.2 Variance of $\Delta K_{th,eff}$

When values of $\Delta K_{th,eff}$ from Table 2 are evaluated it can be noticed that they are higher for tests at R=0.1 than for R=0.7. This seems surprising as the theory predicts only a dependence of $\Delta K_{th,eff}$ on the Young´s modulus and the square root of the burgers vector [31]. The answer to that phenomenon lies is the limited accuracy of the measurement of the crack extension via the potential drop technique. A minimum detectable crack extension was determined to about 2-3 μm due to noise in the signal. At R=0.1 crack closure effects are more pronounced and hinder the crack extension, while at R=0.7 closure effects are strongly reduced and therefore the minimal detectable crack extension can occur at a lower ΔK than for R=0.1.

4.3 Anisotropy of the FCG-Behavior

Comparing the fracture surfaces of the different specimen orientations, one would expect only a small difference in the FCG behavior. However, FCG-data provides a different picture and a microstructural analysis can give a satisfying explanation. When looking at the texture, which is a {100}<011> rotated cube texture, it is expected that cracks propagating in the T-L and L-T system should behave in a similar manner. In both orientations the principal crystallographic fracture planes are the {110}. Only for the 45° orientation a different behavior is expected, since here the cleavage crack planes are {100}. The {100} fracture planes typically show lower fracture toughness values in single crystals than the {110} planes [32]. But the FCG data shows better FCG behavior for the L-T orientation than for T-L, i.e. da/dN-rates for T-L are higher by a factor of about 2-3 than for L-T. So the texture seems to have only an inferior influential role. A more important factor seems to be the grain shape. As described in section 3.2 the microstructure

exhibits pancake-like shaped grains that are elongated parallel to the rolling direction. For the crack propagation this means that cracks have to deviate more from the macro crack growth direction in the L-T system than in the T-L system, see Figure 30. The deviation causes a strong variation of the local loading mode which changes from pure mode I to a mixture of mode I and II, see Figure 31. An increase in the crack deflection angle induces a reduction of the local mode I component, which is the more important contribution for the fatigue crack driving force. Therefore, the crack propagation rate decreases in the case of more pronounced crack deflection. In addition, the roughness of the crack surface and the mode II component can lead to a premature contact of the crack flanks and shield the crack tip, causing a reduced crack growth rate. This effect is commonly referred as roughness induced crack closure (RICC). In the T-L crack system the crack deviation is less pronounced. An aspect ratio of the grains of about 2:1 to 4:1 is in good agreement with the difference in the da/dN-rates between these two crack systems. This assumption is further supported by crack growth rates of the 45° system, which has da/dN-rates somewhere between those two.

An anisotropy can also be found for ΔK_{th} values: for the 2 mm and 1 mm material the L-T orientation shows 20-50 % higher values at R=0.1 and about 10-20 % higher values at R=0.7. Surprisingly this role is reversed for the 100 µm foils. Further investigations addressing this phenomenon is needed.
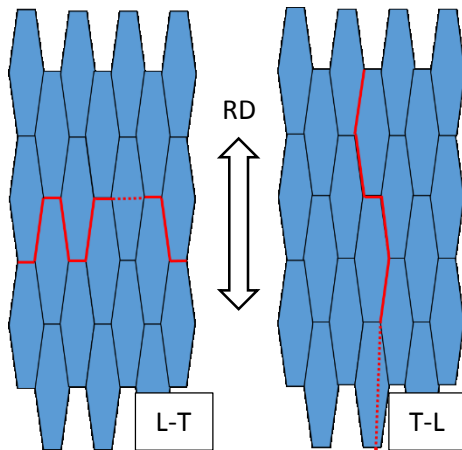
Figure 30: Illustration of the crack path in L-T and T-L samples, please take into account that thickness of the grains is significantly smaller than the depicted length and width. In the L-T crack system (left) cracks deviate more from the principal crack growth direction than in the T-L system (right) leading to lowered da/dN-rates. Dotted red lines indicate transcrystalline fracture, full red lines indicate intercrystalline fracture. The rolling direction (RD) is from top to bottom.

Figure 31: Crack deflection leading to a mixture of mode I and II although the principal loading mode is purely mode I

4.4 Influence of the Load Ratio R

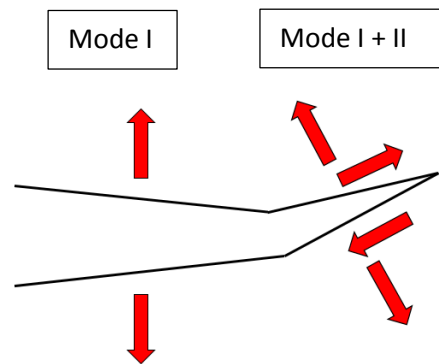From the FCG-experiments it becomes obvious that the load ratio R has a significant influence on the threshold values ΔK_{th} but also on the crack propagation rates da/dN. These differences arise in ductile alloys usually from crack closure effects, which are also called extrinsic effects as they often act behind the crack tip and are therefore not an intrinsic property of the material and can vary with environmental conditions [33]. On the fracture surfaces of specimens tested at R=0.1 an often heavily oxidized fracture surface can be seen. This indicates that oxide induced crack closure (OICC) had occurred and has led to a premature contact of the crack flanks which shielded the crack tip. A big difference of $\Delta K_{th,eff}$ and ΔK_{th} indicate a pronounced cyclic R-curve with a strong OICC. Due to the higher mean stress intensity factor at R=0.7 these effects should be strongly reduced as the crack flanks are further apart and shielding should not be so distinct. Surprisingly, even at R=0.7 all material states exhibited a cyclic R-curve behavior, indicated by the difference of $\Delta K_{th,eff}$ and ΔK_{th}. Fracture surface analysis revealed that parts of the crack faces showed oxidation and hence OICC seemed to have occurred. At R=0.7 plasticity induced crack closure (PICC) seems to have a more significant role. Because of the higher mean stresses, the necking of the samples is more distinctive which has led to delaminations and successively to the formation of secondary cracks. These secondary cracks formed regularly on specimens tested at R=0.7 and only few of them could be seen on specimens tested at R=0.1. Delamination and secondary cracks promote plane stress conditions and this in turn promotes plastic deformation and increases the effect of plasticity induced crack closure. As a consequence, premature contact of the crack flanks has occurred even at R=0.7 and thus shielding of the crack tip is provided.

4.5 Crack Propagation Mechanism

To gain insight on the mechanisms that are responsible for the crack propagation it is helpful to evaluate the slope in the Paris-regime. Since the crack did not propagate for a reasonable length in the 2 mm and 1 mm material this evaluation is limited to the foils with 100 µm thickness. Analysis of the fracture surfaces indicate a reasonable amount of plastic deformation. Plastic deformation at the crack tip can be described by the crack tip opening displacement range ΔCTOD, which can be connected to ΔK using the following formula:

$$\Delta CTOD = \frac{\Delta K^2}{2E\sigma_y} \cdot d_n \tag{10}$$

where d_n is a factor depending on the hardening behavior of the material. It can be shown that this factor is 0.78 for non-hardening materials [34] in plane strain conditions which seems to be a good approximation for the tungsten foils as they show nearly elastic-perfect plastic behavior in tensile tests [23]. However, because of the thin nature of the foils (100 µm) plain stress conditions are prevailing and therefore $d_n=1$ is chosen [34]. In ductile materials fatigue cracks grow by a blunting and re-sharpening process of the crack tip [35]. The crack growth rate is in such case about 1/3*ΔCTOD. A comparison of ΔCTOD and the crack growth rates permits to estimate if a brittle fracture or a ductile behavior dominates the fatigue crack propagation. A ΔCTOD-line can be plotted in the FCG-diagram and compared to FCG-data, as depicted in

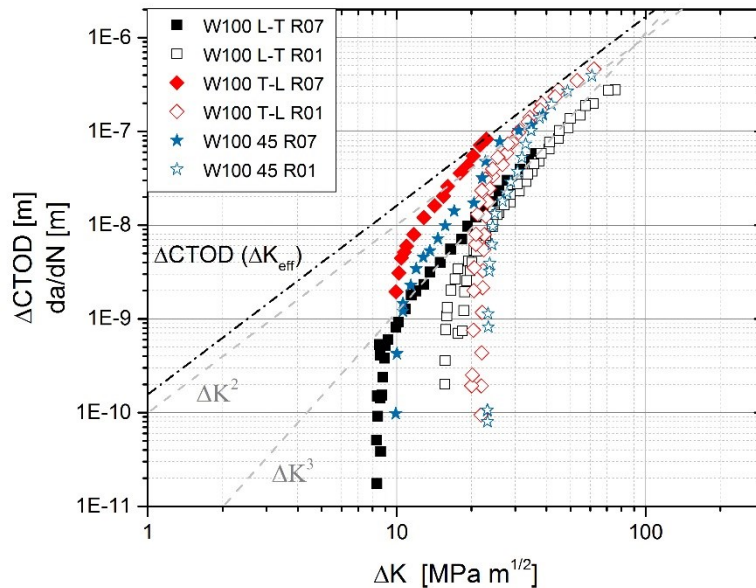

Figure 32: FCG-curves from W 100 µm for all orientations. The black dash-dotted line represents the calculated ΔCTOD values. The gray dashed lines are guide lines for ΔK² ΔK³ and show that the slope of the FCG-data lies closer to 3 than to 2.

Figure 32 (values for tungsten foil were E=405 GPa, σ_y=2100 MPa and d_n=1). As all the data lies underneath the ΔCTOD-line it can be concluded that the dominating mechanism is a blunting and re-sharpening process of the crack tip. However, it is worth noting that the slope in the Paris-regime for all three orientations are somewhere close to 3 and not 2. This indicates that a further mechanism of a degradation in front of the crack tip is taking place. Furthermore, one should take into account that in equation 10 ΔK_{eff} instead of ΔK should be used in order to obtain the crack closure corrected ΔCTOD. Due to the plane stress dominated fatigue crack propagation the crack closure at R=0.1 should be significant. If one assumes that ΔK_{eff}~0.5*ΔK at R=0.1 the calculated ΔCTOD is only somewhat larger than da/dN.

4.6 Frequency Dependence

The result that the da/dN-rates significantly rise by a factor of about 3 when the frequency is lowered from 1 Hz to 0.1 Hz is rather astonishing, see Figure 13. Like all bcc-metals, tungsten possesses a strain-rate sensitivity of the flow stress at low temperatures. Qualitatively, the decrease of the frequency should decrease the local flow stress, when a positive strain-rate sensitivity is assumed. Therefore, ΔCTOD should increase, this may explain a small increase of da/dN (see equation 10). However, an increase by a factor of 3 is not explainable by the change of ΔCTOD induced by the strain-rate sensitivity.

5. Conclusion

In this work the influence of cold rolling on the fatigue crack growth behavior of tungsten sheets was investigated. The most important findings can be summarized as follows:

- Cold rolling to 2 mm thickness is a sufficient degree of deformation to induce a cyclic R-curve behavior with ΔK_{th} reaching values of up to about 23 MPam$^{1/2}$. Further rolling to thinner foils leading to a grain refinement does not significantly change this near threshold behavior.

- Even at higher load ratios (i.e. R=0.7) cyclic R-curve behavior is observable. Due to higher mean stresses necking is more pronounced leading to strong plasticity induced crack closure. At lower load ratios (R=0.1) oxide induced crack closure seems to be the dominating shielding effect.

- The rolling process causes an anisotropy of the FCG behavior. For the 2 mm and 1 mm sheets the L-T orientation exhibits higher values for ΔK_{th} than the T-L orientation. Surprisingly, for the 100 μm foils this role seems to be vice-versa. Although in the Paris-regime the da/dN-rates for the L-T orientation are lower than that of the T-L orientation. This is induced by the pancake-like shaped grains that are elongated parallel to the rolling direction. The texture (which was found to be a rotated cube texture) does not to play a significant role. This is further confirmed as the 45° orientation yields da/dN-rates between T-L and L-T.

- The severe cold rolling to foils of 100 μm thickness leads to a distinctive Paris-regime. This is a result of the significantly increased fracture toughness.

- The controlling mechanism for crack growth seems to be a blunting and re-sharpening process. However, a slope close to 3 in the Paris-regime indicate an additional mechanism such as deformation induced cleavage.

- Lowering the testing frequency drastically increases the crack growth rates of the 100 μm foils. This can in part be explained by the increased ΔCTOD due to the lowered strain-rate. However, further research is needed to give an adequate explanation for the drastic increase of da/dN rates.

Overall it can be concluded that cold rolling significantly improves the FCG behavior of tungsten sheets and make hope for future applications such as cooling pipes. Future experiments are needed to investigate the FCG behavior at elevated temperatures that are close to the operating temperatures. It is also important to gain knowledge on how fatigue cracks propagate in laminated materials (e.g. W-AgCu or W-Cu laminates).

6. Acknowledgments

7. References

[1]   E. Lassner, W.D. Schubert, Tungsten: Properties, Chemistry, Technology of the Elements, Alloys, and Chemical Compounds, 1st ed., Springer, 1999.

[2]   www.plansee.com, (2019).

[3]   J. Reiser, H. Greuner, D.E.J. Armstrong, B.J. Reiser, M. Rieth, M. Anton, W. Hering, A. Hoffmann, J. Hoffmann, H. Leiste, T. Denk, T. Gr, A. Zabernig, T. Mrotzek, R. Pippan, W. Schulmeyer, T. Weing, Tungsten (W) Laminate Pipes for Innovative High Temperature Energy Conversion Systems **, (2014) 491–501. doi:10.1002/adem.201400204.

[4]   www.iter.org, (2020).

[5]   A.A.N. Németh, J. Reiser, D.E.J. Armstrong, M. Rieth, Int . Journal of Refractory Metals and Hard Materials The nature of the brittle-to-ductile transition of ultra fi ne grained tungsten (W) foil, RMHM. 50 (2015) 9–15. doi:10.1016/j.ijrmhm.2014.11.005.

[6]   J. Reiser, J. Hoffmann, U. Jäntsch, M. Klimenkov, S. Bonk, C. Bonnekoh, M. Rieth, A. Hoffmann, T. Mrotzek, Int . Journal of Refractory Metals and Hard Materials Ductilisation of tungsten (W): On the shift of the brittle-to-ductile transition (BDT) to lower temperatures through cold rolling, 54 (2016) 351–369. doi:10.1016/j.ijrmhm.2015.09.001.

[7]   G.A. Geach, J.E. Hugh, The alloy of rhenium with molybdenum or with tungsten and having good high temperature properties, in: Proc. 2nd Plansee Semin., 1955: p. 245.

[8]   R.P. Rama, N.S.V. Nagender, Phase diagrams of binary tungsten alloys, 1991.

[9]   P.L. Raffo, Yielding and Fracture in Tungsten and Tungsten-Rhenium Alloys, J. Less-Common Met. 17 (1969) 133–149.

[10]   A. Luo, D.L. Jacobson, K.S. Shin, Solution softening mechanism of iridium and rhenium in tungsten at room temperature, Int. J. Refract. Met. Hard Mater. 10 (1991) 107–114.

[11]   H. Li, S. Wurster, C. Motz, L. Romaner, Dislocation-core symmetry and slip planes in tungsten alloys : Ab initio calculations and microcantilever bending experiments, Acta Mater. 60 (2012) 748–758. doi:10.1016/j.actamat.2011.10.031.

[12]   B. Gludovatz, S. Wurster, A. Hoffmann, R. Pippan, Int . Journal of Refractory Metals and Hard Materials Fracture toughness of polycrystalline tungsten alloys, RMHM. 28 (2010) 674–678. doi:10.1016/j.ijrmhm.2010.04.007.

[13]   S. Wurster, B. Gludovatz, R. Pippan, Int . Journal of Refractory Metals and Hard Materials High temperature fracture experiments on tungsten – rhenium alloys i, RMHM. 28 (2010) 692–697. doi:10.1016/j.ijrmhm.2010.03.002.

[14]   J.B. Wachtmann, Mechanical Properties of Ceramics, New York: Wiley, 1996.

[15]   R.H. Jones, C.H.H. Jr, Subcritical crack growth processes in SiC / SiC ceramic matrix composites, 25 (2005) 1717–1722. doi:10.1016/j.jeurceramsoc.2004.12.015.

[16]   C. Linsmeier, J. Riesch, Y. Han, Development of advanced high heat flux and plasma-facing materials, (2017).

[17]   J. Riesch, J. Buffiere, T. Ho, ScienceDirect In situ synchrotron tomography estimation of toughening effect by semi-ductile fibre reinforcement in a tungsten-fibre-reinforced tungsten composite system, 61 (2013) 7060–7071. doi:10.1016/j.actamat.2013.07.035.

[18]   J. Riesch, Y. Han, J. Almanstötter, J.W. Coenen, T. Höschen, B. Jasper, P. Zhao, C. Linsmeier, R. Neu, Development of tungsten fi bre-reinforced tungsten composites towards their use in DEMO — potassium doped tungsten wire, Phys. Scr. T167 (2016) 14006. doi:10.1088/0031-8949/T167/1/014006.

[19]   R.Z. Valiev, I. V Alexandrov, Paradox of strength and ductility in metals processed by severe plastic deformation, (2002) 5–8.

[20]   Q. Wei, L.J. Kecskes, Effect of low-temperature rolling on the tensile behavior of commercially pure tungsten, 491 (2008) 62–69. doi:10.1016/j.msea.2008.01.013.

[21]   S. Bonk, J. Reiser, J. Hoffmann, A. Hoffmann, Int . Journal of Refractory Metals and Hard Materials Cold rolled tungsten (W) plates and foils : Evolution of the microstructure, RMHM. 60 (2016) 92–98. doi:10.1016/j.ijrmhm.2016.06.020.

[22]   V. Nikolic, S. Wurster, D. Firneis, R. Pippan, Improved fracture behavior and microstructural characterization of thin tungsten foils, Nucl. Mater. Energy. 9 (2016) 181–188. doi:10.1016/j.nme.2016.06.003.

[23]   H. Materials, S. Bonk, J. Ho, A. Ho, J. Reiser, International Journal of Refractory Metals Cold rolled tungsten (W) plates and foils : Evolution of the tensile properties and their indication towards deformation mechanisms, 70 (2018) 124–133. doi:10.1016/j.ijrmhm.2017.09.007.

[24]   J. Reiser, M. Rieth, A. Möslang, B. Dafferner, A. Hoffmann, X. Yi, D.E.J. Armstrong, Tungsten foil laminate for structural divertor applications – Tensile test properties of tungsten foil, J. Nucl. Mater. 434 (2013) 357–366. doi:10.1016/j.jnucmat.2012.12.003.

[25]   V. Nikolic, S. Wurster, D. Firneis, R. Pippan, Fracture toughness evaluation of UFG tungsten foil, Int. J. Refract. Met. 76 (2018) 214–225. doi:10.1016/j.ijrmhm.2018.06.008.

[26]   B. Gludovatz, S. Wurster, T. Weingärtner, A. Hoffmann, R. Pippan, S. Wurster, T. Weingärtner, A. Hoffmann, R. Pippan, Influence of impurities on the fracture behaviour of tungsten, 6435 (2011). doi:10.1080/14786435.2011.558861.

[27]   L.J. Kecskes, K.C. Cho, R.J. Dowding, B.E. Schuster, R.Z. Valiev, Q. Wei, Grain size engineering of bcc refractory metals : Top-down and bottom-up — Application to tungsten, 467 (2007) 33–43. doi:10.1016/j.msea.2007.02.099.

[28]   J. Reiser, L. Garrison, H. Greuner, J. Ho, T. Weingärtner, U. Jäntsch, M. Klimenkov, P. Franke, S. Bonk, C. Bonnekoh, S. Sickinger, S. Baumgärtner, D. Bolich, M. Ho, R. Ziegler, J. Konrad, J. Hohe, A. Ho, T. Mrotzek, M. Seiss, M. Rieth, A. Möslang, International Journal of Refractory Metals Ductilisation of tungsten (W): Tungsten laminated composites, 69 (2017) 66–109. doi:10.1016/j.ijrmhm.2017.07.013.

[29]   I. Roman, D. Jinchuk, Fatigue Crack Growth In A Sintered Tungsten Alloy, Fatigue Eng. Mater. Struct. 5 (1982) 71–76.

[30]   D. Tabor, P.R.S.L. A, A Simple Theory of Static and Dynamic Hardness Article cited in :, (1948) 247–274. doi:10.1098/rspa.1948.0008.

[31]   R.P. F.O. Riemelmoser, P.Gumbsch, Dislocation Modelling of Fatigue Cracks: An Overview, Mater. Trans. 42 (2001).

[32]   J. Riedle, P. Gumbsch, H.F. Fischmeister, Cleavage Anisotropy in Tungsten Single Crystals, (1996).

[33]   R.O. Ritchie, Mechanisms of fatigue-crack propagation in ductile and brittle solids, (2000) 55–83.

[34]   C.F. Shih, Relationships Between The J-Integral And The Crack Opening Displacement For Stationary And Extending Cracks, J. Mech. Phys. Solids. 29 (1981) 305–326.

[35]   R. Pippan, C. Zelger, E. Gach, C. Bichler, H. Weinhandl, On the mechanism of fatigue crack propagation in ductile, Fatigue Fract. Eng. Mater. Struct. i (2010) 1–16. doi:10.1111/j.1460-2695.2010.01484.x.